

# Nanoscale characterisation of model Ni-Mo catalyst active phases

**Jonas Elmroth Nordlander**

Degree Project in Materials Chemistry, 2022  
Department of Chemistry  
Lund University  
Sweden

30 ECTS credits



**LUND**  
UNIVERSITY



# Nanoscale characterisation of model Ni Mo catalyst active phases

Jonas Elmroth Nordlander



**LUND**  
UNIVERSITY

Degree Project in Materials Chemistry

2022

30 hp

**Head Supervisor:**

Carl Martin Ek Rosén,

Centrum for Analysis and Synthesis  
NanoLund,  
Lund University

Lund University  
Department of Chemistry  
Centre for Analysis and Synthesis  
P.O. Box 124  
SE-221 00 Lund, Sweden

## Populärvetenskaplig sammanfattning

För att möjliggöra omställningen från fossila kolväten har bioolja identifierats som ett viktigt verktyg. Bioolja refererar till ämnen med liknande egenskaper som traditionellt petroleum, men som produceras genom kontrollerad förbränning (pyrolys) av jord- och skogsbruksavfall. Bioolja har stor potential, eftersom dess kemisk-fysikaliska likhet till de fossila kolväten som redan används som bränsle och råvara för den kemiska industrin signifikant skulle minska de kostnader och svårigheter som förknippas med övergången.

För att bioolja ska bli gångbart som råvara och bränsle måste det emellertid genomgå en process som kallas *katalytisk hydrodeoxygenering*. En viktig komponent i denna process är nickel-molybden-katalysatorer, som underlättar reaktionen och gör den mer specifik, vilket gör att den industrikemiska processen kräver mindre energi.

För att göra katalysatorerna så effektiva som möjligt krävs god förståelse för hur den s.k. *aktiva fasen*, i detta fall nickel-molybdenoxid, beter sig. Denna oxid kan förekomma i två former,  $\alpha$  och  $\beta$ , där  $\beta$ -formen är den form som ger effektivast katalysator, medan  $\alpha$ -formen är den mest stabila.

Traditionellt sett har det emellertid på grund av designen i kommersiella katalysatorer varit svårt att studera den aktiva fasen direkt. Med en metod som kallas ”spark discharge generation”, har det dock blivit möjligt att skapa mycket små nanopartiklar av nickel-molybden som påminner om hur man tror den aktiva fasen i kommersiella katalysatorer ser ut. Kortfattat går metoden ut på att med hjälp av snabba gnisturladdningar mellan två nickel-molybdenelektroder förånga en liten del av elektroden. Denna metallånga kondenserar sedan ned till nanometerstora metallpartiklar som sedan kan analyseras i elektronmikroskop eller med hjälp av röntgendiffraktion. Partiklarna kan även oxideras för att bilda den aktiva fasen.

I detta arbete genereras partiklar med ett nickel-molybdenförhållande kring 30:70, vilket motsvarar förhållandet i många kommersiella katalysatorer. Elektronmikroskopi och röntgendiffraktion används för att analysera sådana partiklars lämplighet som modellsystem för den aktiva fasen i riktiga katalysatorer. Dessa två experimentella tekniker utgör goda komplement till varandra, eftersom röntgendiffraktion kan ge ett genomsnitt av strukturen i ett prov, medan elektronmikroskopi är lämpat för att studera strukturen på en lokal nivå, till exempel i enskilda partiklar.

Resultaten indikerar att partiklarna när de oxideras förlorar en del av sitt molybden, och går ned mot en nickel-molybdenförhållande på 45:55-40:60. Resultatet ger även indikationer på att  $\beta$ -formen av nickel-molybdenoxid bildas preferentiellt när mycket små nickel-molybdenpartiklar oxideras, istället för den annars mer stabila  $\alpha$ -fasen. Eftersom många små partiklar har högre katalytisk aktivitet än samma vikt av få stora, skulle tidigare resultat där  $\beta$ -formen visat högre aktivitet kunna härledas till att den aktiva fasen är bättre spridd i katalysatorn. Slutligen ger röntgendiffraktionsresultat indikationer på att en ny nickel-molybdenfas bildas när partiklarna genereras, men dess struktur och ursprung är ännu oklara.

Sammanfattningsvis utgör partiklarna ett lämpligt modellsystem för kommersiella katalysatorer med upp till ett visst överskott av molybden.

## Abstract

An important stepping stone in transitioning from a fossil-fuel based transportation system is the production of bio-fuels such as bio-oils. For bio-oils to be commercially viable, catalytic upgrading via hydrodeoxygenation is required, typically using Ni-Mo oxide or sulfide catalysts. To optimise such processes, a thorough understanding of the catalyst is required. Spark discharge generation (SDG) of nanoparticles allows for a potentially useful model system for such catalyst due to the possibility of creating particles with a known composition, size distribution, and surface concentration.

This report aims to characterise the oxidation and reduction of SDG-generated Ni-Mo nanoparticles and determine their suitability as model systems for the active phase of commercial Ni-Mo catalysts.

Ni-Mo nanoparticles were deposited onto SiO<sub>x</sub> wafers or SiN TEM grids using an in-house spark ablation device. Characterisation was carried out using X-ray diffraction, HRTEM imaging, and compositional analysis with STEM-XEDS.

The as-deposited particles exhibit Janus morphologies with a pure Mo part and a Ni-Mo part with structure and composition not expected from the Ni-Mo equilibrium diagram. Oxidation of isolated particles generated particles consisting mainly of  $\beta$ -NiMoO<sub>4</sub>; in contrast, oxidation of bulk powders generated mainly  $\alpha$ -NiMoO<sub>4</sub>, while reduction followed previously published results on the reduction of NiMoO<sub>4</sub>. Upon oxidation, the Mo percentage in the particles decreased, which can be attributed to evaporation of MoO<sub>3</sub>.

Previous literature indicating higher activity of supported Ni-Mo catalysts with  $\beta$ -NiMoO<sub>4</sub> compared to  $\alpha$ -NiMoO<sub>4</sub> may be attributed to such catalysts having smaller active phase domains and less sintering. SDG-generated Ni-Mo particles can be used as a model catalyst active phase for Ni-Mo catalysts with less than ca 60 at. % Mo.

**Keywords:** Ni-Mo catalysts, hydrodeoxygenation, TEM, PXRD

## **Acknowledgements**

The author wishes to thank all six (!) supervisors on the project: Martin Ek Rosén, Maria Messing, Sara Blomberg, Pau Ternero, David Wahlqvist, and Marie Bermeo Vargas, for their valuable advice and help, both concerning practical matters and theoretical questions, without which this work would not have been possible. Also deserving thanks are the other members of Maria's group: Knut Deppert, Markus Snellman, Namsoon Eom, Mehran Sedrpooshan, Linnea Jönsson *et ceteri*, for valuable discussions and generous amounts of *fika*. A final mention goes to Julia-Maria Hübner for help with *ab initio* structural indexation.

# Contents

1. List of abbreviations.....	1
2. Introduction.....	2
3. Background.....	4
3.1. The Ni-Mo system.....	4
3.1.1. Phases and crystal structures.....	4
3.1.2. Oxidation and reduction in the Ni-Mo system.....	9
3.1.3 Hydrodeoxygenation and Ni-Mo catalysts.....	10
3.3. Spark discharge generation and the differential mobility analyzer (DMA).....	11
3.3. Powder X-ray diffraction (PXRD).....	12
3.4. Transmission electron microscopy (TEM).....	14
3.4.1. Principles of TEM.....	14
3.4.2. Artifacts in TEM.....	15
4. Methods.....	16
4.1. Sample synthesis and preparation.....	16
4.2. Oxidation of particles.....	17
4.3. Reduction of particles.....	17
4.4. PXRD.....	17
4.5. Ex situ CTEM and STEM study.....	17
5. Results.....	18
5.1 General.....	18
5.2. As-deposited nanoparticles.....	18
5.2. Oxidised nanoparticles.....	26
5.3. Reduced nanoparticles.....	33
6. Discussion.....	39
7. Summary and Conclusions.....	41
8. Outlook.....	42
9. References.....	43
10.A. Appendix A – Parabolic rate laws.....	49
10.B. Appendix B – Gauss’s approximation formula and error propagation to atomic percentages.....	50

## 1. List of abbreviations

CTEM – Conventional TEM (*qui vide infra*).

EDX – energy dispersive X-ray analysis.

ETEM – environmental TEM.

FOM – figure of merit.

HDO – hydrodeoxygenation.

HRTEM – high resolution TEM.

PXRD – powder XRD (*qui vide infra*).

SA(E)D – selected area (electron) diffraction.

STEM – scanning transmission electron microscopy.

TEM – transmission electron microscopy/microscope.

X@Y – core shell structure with a core consisting of X and a shell consisting of Y.

XEDS – see EDX.

XPS – X-ray photoelectron spectroscopy.

XRD - X-ray diffraction.

## 2. Introduction

The production of renewable fuels has been identified as a key technology for achieving net zero emissions of CO<sub>2</sub> and combatting ongoing climate change [1]. One form of renewable fuel that has received considerable attention for the last three decades is bio-fuels [2-5], i.e., fuels produced from biological renewable sources, mainly plant matter. Especially the utilisation of secondary biomass, such as cereal straw and other agricultural by-products, waste, or forestry products, has been a topic of research, as such sources of bio-fuels do not compete directly with the production of food [4].

One route towards the production of bio-fuel is thermochemical production of bio-oil [6]. The main advantage over other routes is the greater ease of integration of bio-oils into the present chemical refinery infrastructure, as the product is broadly similar to petroleum feedstocks [7]. Compared to petroleum, bio-oil is however still characterised by much higher heterogeneity from a chemical perspective, as well as a higher average degree of oxidation due to functionalisation of carbon, chief among which is oxygen [7]. The presence of oxygen-rich moieties such as carboxylic acid functions poses obstacles to the storage and usage of fractionated biomass in e.g. traditional combustion engines due to potentially corrosive properties [7], while the higher degree of oxidation means such fuels have a lower energy density than comparable fossil fuel counterparts [7]. The deoxygenation through catalytic hydrodeoxygenation (HDO) of biomass is therefore an important topic for the production of bio-fuels.

Ni- and Co-promoted Mo catalysts (X-Mo, X = Ni, Co) in oxide or sulfide form have been previously identified as being suitable for HDO of bio-oils [8, 9]. Although other catalysts have been considered in the literature, such as supported Pd or other noble metals [9], the relatively lower cost of X-Mo-type catalysts [10, 11] and the already existing production volume due to their heavy use in industrial hydrodesulfurisation of fossil feedstocks [12], make them an attractive choice from an industrial-economic perspective.

X-Mo catalysts are usually prepared as X-Mo oxide nanoparticles deposited on a porous Al<sub>2</sub>O<sub>3</sub> support [11]. For the Ni-Mo system, this means some combination of NiO, NiMoO<sub>4</sub>, and MoO<sub>3</sub>, depending on the Ni:Mo ratio used [13]. Previous publications indicate that supported catalysts prepared such that the meta-stable  $\beta$ -polymorph of NiMoO<sub>4</sub>, rather than the thermodynamically stable  $\alpha$ -NiMoO<sub>4</sub>, is present, show higher catalytic activity [14-16], and that this effect persists upon conversion to the sulfide [15]. However, direct study of the as-prepared active phase has been hampered by its dispersed nature in the support matrix. More specifically, any sample of the catalyst will have the support phase as its major component, meaning that any signal (or image) will be dominated by the support phase rather than the active phase.

Recently, Blomberg et al. synthesised 25 nm Ni-Mo nanoparticles using spark ablation and differential mobility analyser (DMA) size selection, with XPS results indicating good agreement between oxidation states of the oxidised particles and commercial catalysts [17]. Nanoparticles generated via spark ablation could therefore offer a powerful tool for modelling the behaviour of the active phase of supported Ni-Mo catalysts and directly observing morphological changes in the active phase.

In this report, an analysis of the structure of spark-ablation synthesised Ni-Mo nanoparticles is presented, both as-deposited, oxidised, and oxidised with subsequent reduction, in order to determine their suitability as a model system for the Ni-Mo catalyst active phase. PXRD and TEM results indicate that for small oxidised particles, the formation of the  $\beta$ -polymorph of NiMoO<sub>4</sub> may be favoured over the otherwise thermodynamically stable  $\alpha$ -polymorph. The reduction of the particles follows previous results for the reduction of NiMoO<sub>4</sub>, while the as-deposited particles show indications of having been quenched into a non-equilibrium crystal structure.

## 3. Background

### 3.1. The Ni-Mo system

To understand the oxidation and reduction phenomena in the studied model system, an overview of the phases in the Ni-Mo system, as well as of previous studies on the oxidation and reduction of Ni-Mo alloys and oxides, is presented.

#### 3.1.1. Phases and crystal structures

At ambient conditions, the Ni-Mo system forms five solid phases: the terminal, substitutional Ni- and Mo-rich solid solutions, and intermetallic phases  $\beta$ ,  $\gamma$ , and  $\delta$  [18, 19]. The solubility of Ni in BCC Mo is highly limited, whereas the solubility of Mo in FCC Ni is ca 10.5 % [18]. Among the intermetallics,  $\beta$  and  $\gamma$  represent stoichiometric  $\text{Ni}_4\text{Mo}$  and  $\text{Ni}_3\text{Mo}$ , respectively, while  $\delta$  represents a non-stoichiometric phase with composition ranging between 48-52 at% Ni [18]. Details of the crystal structures of the respective phases can be found in Table 1. The crystal structures of the intermetallics can be found in Figure 1.

Table 1: Crystal structures for the different solid phases of the Ni-Mo system. For the terminal solutions, lattice parameters are given for the pure metal.

Phase	Structure/Crystal system	Space group	Lattice parameter(s)
Terminal Ni	FCC (Cubic)	$\text{Fm}\bar{3}\text{m}$ (225)	$a_0 = 3.499 \text{ \AA}$ [20]
Terminal Mo	BCC (Cubic)	$\text{Im}3\text{m}$ (229)	$a_0 = 3.142 \text{ \AA}$ [20]
$\beta$ ( $\text{Ni}_4\text{Mo}$ )	Tetragonal [21]	$\text{I}4/\text{m}$ (87) [19]	$a_0 = 5.720 \text{ \AA}$ , $c_0 = 3.564 \text{ \AA}$ [21]
$\gamma$ ( $\text{Ni}_3\text{Mo}$ )	Orthorhombic [19]	$\text{Pmmn}$ (59) [19]	$a_0 = 5.064 \text{ \AA}$ , $b_0 = 4.223 \text{ \AA}$ , $c_0 = 4.449 \text{ \AA}$ [19]
$\delta$ (non-stoichiometric, $\approx \text{NiMo}$ )	Orthorhombic [22, 23]	$\text{P}2_12_12$ (19) [23]	$a_0 = 9.108 \text{ \AA}$ , $b_0 = 9.108 \text{ \AA}^1$ , $c_0 = 8.852 \text{ \AA}$ [22, 23]

Nickel forms two oxides, NiO and  $\text{Ni}_2\text{O}_3$ . NiO has a simple rock-salt structure [24] and has been well-characterised for decades. In contrast,  $\text{Ni}_2\text{O}_3$  easily decomposes to NiO upon heating, and only within the last decade has it been possible to definitely characterise it in its anhydrous state, via synthesis and characterisation of  $\text{Ni}_2\text{O}_3$  nanoparticles [25]. It crystallises in a monoclinic crystal system built up out of corner-sharing  $\text{NiO}_4$  tetrahedra [26]. The structures are shown in Figure 2.

Mo similarly forms two main oxides,  $\text{MoO}_3$  and  $\text{MoO}_2$  [27]. Additionally, a number of intermediate crystalline shear  $\text{Mo}_n\text{O}_{3n-1}$  and  $\text{Mo}_n\text{O}_{3n-2}$  oxides can be formed [28]. The only thermodynamically stable form of  $\text{MoO}_3$  is  $\alpha$ - $\text{MoO}_3$ , an orthorhombic structure consisting of

<sup>1</sup>  $a_0$  and  $b_0$  are identical to measurement precision as presented in the cited reference, but they are not exactly the same judging by diffraction patterns, and the structure remains orthorhombic.

sheets of edge- and corner-sharing  $\text{MoO}_6$  octahedra (see Figure 2) [27]; however, at ambient conditions two meta-stable polymorphs ( $\beta$  and  $h$ ) exist with monoclinic and hexagonal symmetry, respectively [27]. Both metastable polymorphs decompose to  $\alpha\text{-MoO}_3$  at temperatures above 400 °C [29, 30].

$\text{MoO}_3$  is easily reduced to  $\text{MoO}_2$  through reduction with hydrogen; this is a step in one of the more common procedures for the production of metallic Mo [31, 32]. This reaction is generally thought to proceed via the formation of  $\text{Mo}_4\text{O}_{11}$  when the reduction is carried out above 450 °C [31].  $\text{MoO}_2$  itself crystallises in a distorted rutile structure, with the central metal atoms in each  $\text{MoO}_6$  polyhedron being alternately displaced nearer and further from one another so as to form pairs, resulting in a monoclinic unit cell, shown in Figure 2 [33]. This structure is also known as the  $\text{MoO}_2$  structure.

Nickel and molybdenum additionally form a mixed oxide in the form of  $\text{NiMoO}_4$  or nickel molybdate. It occurs in two polymorphs: the low temperature  $\alpha\text{-NiMoO}_4$  (Figure 2) polymorph and high temperature  $\beta\text{-NiMoO}_4$ , which are distinguished primarily by the coordination of the Mo(VI), which is octahedral in the  $\alpha$ -phase but tetrahedral in the  $\beta$ -phase [16, 34].  $\alpha\text{-NiMoO}_4$  converts to  $\beta\text{-NiMoO}_4$  at approximately 690 °C, but the formed  $\beta\text{-NiMoO}_4$  is thereafter (meta-)stable until 180 °C [35]. The  $\beta$ -phase can also be stabilised by the presence of excess Ni in a mixed-oxide material, however transiently, and has furthermore been identified as present in commercial  $\text{NiMo}/\text{Al}_2\text{O}_3$  hydrotreating catalysts [35], together with  $\text{MoO}_3$  [36].

In addition to the oxides presented above, molybdenum also forms the sulfide molybdenum disulfide ( $\text{MoS}_2$ ) which is believed to be the active phase in sulfidated Ni-Mo catalysts [12], as discussed in more detail in section 3.1.3. It has a characteristic layered structure where each layer consists of Mo(IV) centres coordinating a trigonal prism of sulfide ions, each layer being bound to the others via van der Waals forces. [37]. Depending on how the layers are stacked, the sulfide has two polymorphs at ambient conditions: 2H- $\text{MoS}_2$  with hexagonal symmetry, and 3R- $\text{MoS}_2$  with rhombohedral symmetry [37].

A summary of the structure of some of the more important oxides mentioned above, as well as that of  $\text{MoS}_2$ , can be found in Table 2.

Table 2: Crystal structures for different Ni, Mo, and Ni-Mo oxides.

Oxide	Crystal system/ Structure	Space group	Lattice parameter(s)
NiO	Cubic (Rock-salt) [24]	Fm $\bar{3}$ m (225)	$a_0 = 4.17 \text{ \AA}$ [24]
Ni <sub>2</sub> O <sub>3</sub>	Monoclinic [26]	Cc (9) [26]	$a_0 = b_0 = 5.492 \text{ \AA}$ , $c_0 = 5.989 \text{ \AA}$ $\alpha = \beta = 61.930^\circ$ , $\gamma = 60.952^\circ$ [26]
$\alpha$ -MoO <sub>3</sub>	Orthorhombic (MoO <sub>3</sub> structure) [27]	Pbnm (62) [38]	$a_0 = 3.963 \text{ \AA}$ , $b_0 = 13.855 \text{ \AA}$ , $c_0 = 3.696 \text{ \AA}$ [38]
$\beta$ -MoO <sub>3</sub>	Monoclinic [27, 39]	P2 <sub>1</sub> /c (14)[40]	$a_0 = 7.122 \text{ \AA}$ , $b_0 = 5.374 \text{ \AA}$ , $c_0 = 5.565 \text{ \AA}$ $\beta = 91.88^\circ$ [39]
h-MoO <sub>3</sub>	Hexagonal [27, 30]	P6 <sub>3</sub> (173) [41]	$a_0 = 10.53 \text{ \AA}$ , $c_0 = 14.918 \text{ \AA}$ [30]
MoO <sub>2</sub>	Monoclinic (MoO <sub>2</sub> structure) [33]	P2 <sub>1</sub> /c (14) [33]	$a_0 = 5.584 \text{ \AA}$ , $b_0 = 4.842 \text{ \AA}$ , $c_0 = 5.608 \text{ \AA}$ $\beta = 120.94^\circ$ [33]
$\alpha$ -NiMoO <sub>4</sub>	Monoclinic [34]	C2/m (12) [34]	$a_0 = 9.564 \text{ \AA}$ , $b_0 = 8.732 \text{ \AA}$ , $c_0 = 7.6483 \text{ \AA}$ $\beta = 114.26^\circ$ [34]
$\beta$ -NiMoO <sub>4</sub>	Monoclinic [42]	C2/m (12) [42]	$a_0 = 10.094 \text{ \AA}$ , $b_0 = 9.203 \text{ \AA}$ , $c_0 = 6.996 \text{ \AA}$ $\beta = 107.17^\circ$ [42]
3R-MoS <sub>2</sub>	Trigonal [37]	R3m (160) [37]	$a_0 = b_0 = 3.163 \text{ \AA}$ , $c_0 = 18.370 \text{ \AA}$ , $\gamma = 120^\circ$ [37]
2H-MoS <sub>2</sub>	Hexagonal [43]	P6 <sub>3</sub> /mmc (194) [43]	$a_0 = b_0 = 3.160 \text{ \AA}$ , $c_0 = 12.294 \text{ \AA}$ , $\gamma = 120^\circ$ [43]

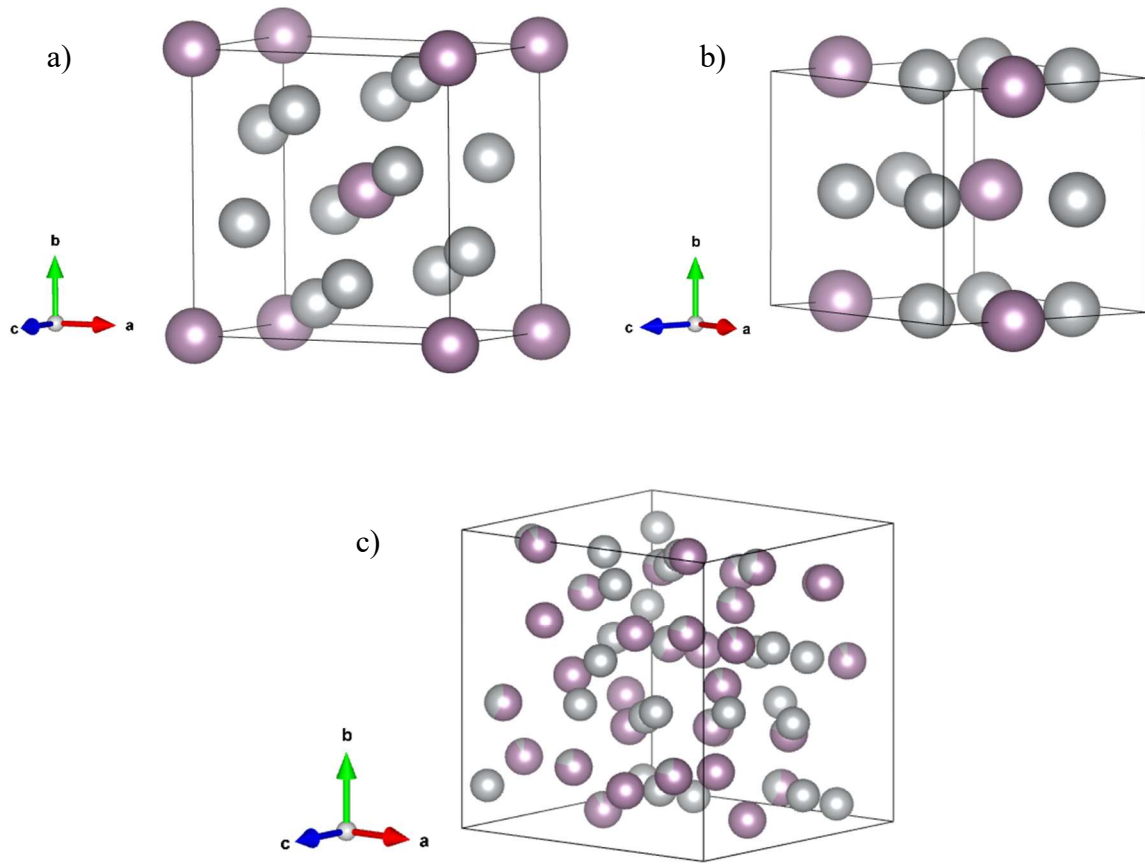


Figure 1: Crystal structures of  $Ni_3Mo$  (a),  $Ni_4Mo$  (b) and  $NiMo$  (c). Based off [44] (a), [21] (b), and [23] (c).

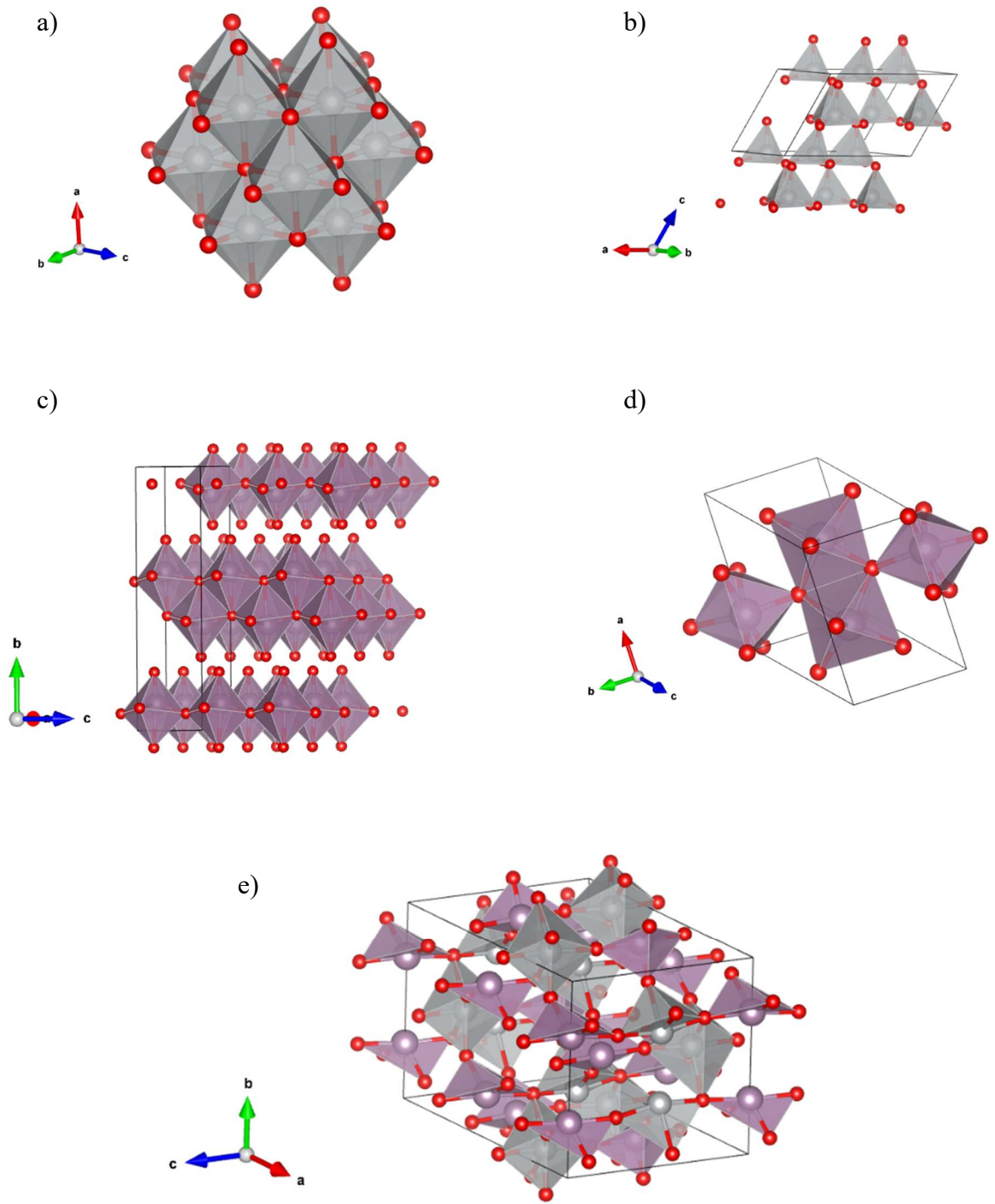


Figure 2: Crystal structures of  $\text{NiO}$  (a),  $\text{Ni}_2\text{O}_3$  (b),  $\text{MoO}_3$  (c),  $\text{MoO}_2$  (d), and  $\alpha\text{-NiMoO}_4$  (e). Based off [45] (a), [26] (b), [38] (c), [46] (d), and [34] (e).

### 3.1.2. Oxidation and reduction in the Ni-Mo system

The oxidation of Ni has been well studied at high temperatures ( $>1000\text{ }^{\circ}\text{C}$ ) [47, 48] where it conforms well to typical parabolic regimes [49] (see also appendix A). At lower temperatures, the oxidation behaviour seems to be highly dependent on the pre-treatment of the sample, producing rate constants differing by as much as four orders of magnitude, before settling to a new parabolic regime below ca  $600\text{ }^{\circ}\text{C}$  [49]. For the oxidation of small particles (diameter = 9, 26, 98 nm) Railsbach et al. found that as oxidation proceeds, a central void forms, creating “vacuum@NiO” particles via the Kirkendall effect [50].

The oxidation of molybdenum and many low-Mo alloys has been thoroughly researched, as molybdenum is important as an alloying element in many high-temperature alloys. For pure molybdenum at ambient conditions, the main oxidation process is the formation of  $\alpha\text{-MoO}_3$ , with formation of  $\text{MoO}_2$  only occurring directly at very low partial pressures of oxygen [51]. Notably,  $\alpha\text{-MoO}_3$  exhibits fairly high volatility above  $600\text{ }^{\circ}\text{C}$  [51, 52], as well as an unusually low melting point at  $795\text{ }^{\circ}\text{C}$  [51, 53]. Both of these contribute to the phenomenon of “catastrophic oxidation” observed in high-temperature Mo alloys, whereby the eventual formation of liquid  $\text{MoO}_3$  drastically increases oxygen diffusivity through the system, causing rapid and catastrophic failure of objects made from these alloys [54].

The oxidation characteristics of Ni-Mo alloys with Mo contents above a few percent is poorly described in the literature; to the best of the author’s knowledge, it is limited to a single study by Brenner et al. in 1955, who studied NiMo alloys with up to 20 at% Mo at between ca  $790\text{-}1200\text{ }^{\circ}\text{C}$  [55]. For such alloys, oxide formation was found to proceed via the formation of an outer layer of NiO encapsulating a layer of  $\text{NiMoO}_4$ , in turn encapsulating the bulk NiMo containing dissolved  $\text{MoO}_2$  [55]. The  $\text{NiMoO}_4$  was reported to be stable up to  $1150\text{ }^{\circ}\text{C}$ , at which point it decomposed to release volatile  $\alpha\text{-MoO}_3$  [55].

The reduction of  $\alpha\text{-NiMoO}_4$  is believed to preferentially proceed via Ni sites on the surface of the oxide [56]. The lower reduction temperature of mixed Ni-Mo oxides compared to pure  $\text{MoO}_3$ , e.g.,  $630\text{ }^{\circ}\text{C}$  for a 79 % Ni mixed oxide compared to  $735\text{ }^{\circ}\text{C}$  for pure  $\text{MoO}_3$  [13], suggests that Ni further facilitates the reduction of Mo in the mixed oxide [13, 57]. In an experiment on  $\text{NiMoO}_4$  nanorods, Patil et al. found that this led to the formation of particles consisting of an Ni-rich Ni-Mo alloy deposited on a porous Mo-rich oxide matrix. While SAED patterns were consistent with the Ni terminal solid solution, the overlap between the various possible Mo-rich oxides hampered closer identification of these [56].

### 3.1.3 Hydrodeoxygenation and Ni-Mo catalysts

Hydrodeoxygenation (HDO) refers to the removal of oxygen-containing moieties in hydrocarbon mixtures using  $H_2$ , increasing the calorific value of hydrocarbon fuels by reducing the oxidation state of the carbon [6, 11]. Together with hydrodenitrogenation (HDN), hydrodesulfurisation (HDS), and similar heteroatom-removing processes under the umbrella of catalytic hydrotreating, HDO has long been used by the petroleum industry for upgrading fuel products [6, 11].

While noble metals such as Pd, Pt, and Ru show high activity for HDO [58], for reasons of cost and availability, traditional HDO catalysts are typically Ni-Mo or Co-Mo catalysts supported on porous alumina [11]. The Ni-Mo catalysts are typically prepared by co-precipitation of Ni-Mo oxides via impregnation of the support with a solution of Ni and Mo oxides [59]. The solvent is then evaporated and the catalyst calcined between 400 and 600 °C [60], producing, ideally [61], well-dispersed Ni and Mo oxides on the support [59-61].

The dispersed Ni-Mo phase has been shown experimentally to be catalytically active in its as-deposited oxide state, but also in reduced form or as a sulfide (NiMoS) [62]. The traditional and most well-researched active phase is the sulfided form, in part because of higher HDO activity compared to the oxide and reduced form [62], but also because the sulfur content of many commercial crude oils induces the formation of the sulfided form on its own [6]. Accordingly, the sulfided form of the catalyst is the most well-studied in terms of catalytic mechanism.

The mechanism usually proposed for the sulfided catalyst can briefly be described as follows: the sulfidation induces the formation of  $MoS_2$  nanoclusters at the active sites [12]. At S vacancies on the surfaces, heteroatom-containing moieties of the organic feed as well as hydrogen are able to adsorb chemically [7]. The hydrogen then reacts with the organic feed via a carbocation intermediate, whereupon the vacancy is filled with the heteroatom. The heteroatom thereafter leaves the vacancy upon hydrogenation from  $H_2$  in the surrounding reaction mixture. The role of Ni is suggested to mainly lie in increasing the number of such vacancies by replacing some of the Mo, disrupting the charge balance and forcing more Mo atoms to become coordinatively unsaturated [63]. For the native oxide and reduced oxide catalysts, the mechanism is proposed to be similar, but proceeding via oxygen vacancies on the oxide surface instead [64]. The primary function of reducing the catalyst is then to increase the number of oxygen surface vacancies by forming Mo(IV) on the surface of an otherwise Mo(VI)-populated lattice [64].

The catalytic activity of NiMo catalysts has furthermore consistently been shown to depend on the polymorph of  $NiMoO_4$  present in the system, with  $\beta$ - $NiMoO_4$  resulting in a higher catalytic activity than  $\alpha$ - $NiMoO_4$  [14-16], even for catalysts that subsequently undergo sulfidation [15].

### **3.3. Spark discharge generation and the differential mobility analyzer (DMA)**

Spark ablation allows for the generation of small metallic particles of a relatively well-defined composition. As such, controlled deposition onto selected substrates allows for the creation of high-surface area samples, in principle suitable for characterisation of the active phase in heterogeneous catalysts. A brief overview of the spark ablation therefore follows below.

Any capacitor has a breakdown voltage, which is the voltage above which the dielectric medium that separates its halves becomes conductive, resulting in a discharge of the accumulated charge. In spark discharge generation of particles, a capacitor is constructed from rods of the desired particle material with air (or another gas) as the dielectric medium. If this capacitor is then repeatedly pulsed to its breakdown voltage, a spark will be discharged across the gap between the rods. This results in partial vaporisation of the rods. By removing the vapours in a carrier gas such as N<sub>2</sub>, they can then be allowed to coalesce into nanoparticles of the desired material [65].

However, such nanoparticles will naturally have a distribution of sizes, which for certain applications is undesirable. The generated nanoparticles can be filtered for size by charging them and using a differential mobility analyser (DMA). A DMA consists of a cylinder with an internal central rod, between which an electric field is applied. At one end, the particle aerosol is entered. As the particles move through the space of the DMA, they will be deflected according to their charge and volume. By tuning the electric field and only gathering the particles that exit the cylinder at a certain deflection, the particles can be filtered for size [66].

### 3.3. Powder X-ray diffraction (PXRD)

X-ray diffraction has been a staple of the structural characterisation of materials for well over a hundred years, and is often summarised by Bragg's law:

$$n\lambda = 2d_{hkl}\sin(\theta), \quad (1)$$

where  $\lambda$  is the wavelength of the X-ray,  $n$  an integer,  $d_{hkl}$  the spacing of the reflecting planes, and  $\theta$  the Bragg angle of diffraction (corresponding to *half* the angular change in propagation direction of the beam) [67].

If the material to be characterised is available as a single crystal, the direction and intensity of the diffraction spots that arise can be directly related to the symmetry of the crystal lattice via the concept of reciprocal space. Reciprocal space is the space of "allowed" propagation direction changes in the crystal lattice ("allowed" in the sense that they lead to constructive interference and thus a measurable exit wave), and the reciprocal lattice so formed is related to the real-space lattice via the Fourier transform. Crucially, the reciprocal lattice contains symmetry information about the real-space lattice. By rotating a single crystal and observing the changes in diffraction spots, different sections of the reciprocal lattice are viewed, which can then be used to reconstruct the symmetry and unit cell of the real-space lattice [67].

However, many important materials are hard or impossible to synthesize as large enough single crystals that such experiments are possible. Powder X-ray diffraction instead uses a polycrystalline sample; the resulting diffraction pattern is essentially a projection of reciprocal space onto a single axis (usually presented as the diffraction angle  $2\theta$ ) [68]. This entails the loss of some degree of symmetry information. However, determination of the crystal structure from powder data is still possible, although the system of equations needed becomes indeterminate, and so numerical methods are required [69]. For high symmetry structures, such methods can be carried out by hand, but for lower symmetry cases, computer methods are usually required [70].

One method for *ab initio* structural indexation is DICVOL06. In this algorithm, a unit cell is assumed within a volume interval on the basis of the first three (for assumed systems of orthorhombic symmetry or higher) [69], four (for systems of monoclinic symmetry, or six (for systems of triclinic symmetry) peaks [71], indexing the peaks with arbitrary indices. The square of the reciprocal space vector length  $|g_{hkl}|^2 = f(a, b, c, \alpha, \beta, \gamma, h, k, l) = Q_{hkl}$  is computed for all peaks and compared with the observed peaks  $Q_{obs}$ . If all  $Q_{hkl}$  fall within the experimental uncertainty in  $Q_{obs}$ , the solution is accepted, and further division of the volume interval occurs to search for additional solutions. This process is iterated until the program reaches a set maximum allowed unit cell volume determined by the user [69].

The solutions so achieved are then ranked using the de Wolff figure of merit  $M_{20}$  [69], which is defined as follows [72]:

$$M_{20} = \frac{Q_{20}}{2N_{20}\bar{\epsilon}}, \quad (2)$$

where  $Q_{20}$  is the Q-value of the twentieth experimental line,  $N_{20}$  is the number of calculated Q-values less than  $Q_{20}$ , and  $\bar{\epsilon}$  is the average discrepancy (in units of  $L^{-2}$ ) between the calculated and observed lines.

A further feature of PXRD is the line broadening that occurs for materials with small crystalline domain sizes. For single-crystal diffraction, the crystal lattice can be considered a periodic function that covers the entirety of  $\mathbb{R}^3$ , meaning that each reciprocal lattice point becomes approximately infinitely small, i.e., a true zero-dimensional object [67]. As the average crystal grain size decreases (as is the case in most polycrystalline samples), however, the reciprocal lattice points broaden into spheres [67]. In PXRD, this manifests as a contribution to the line width in each reflection; the broader a peak is, the smaller are the domains that contribute to it [73]. However, other parameters such as imperfections in the instrumental set-up also contribute to line broadening [73]. Only if the instrumental line broadening is known can the line width be used to determine the average grain size quantitatively.

### 3.4. Transmission electron microscopy (TEM)

Transmission electron microscopy is a powerful tool for high-resolution local structural and compositional determination, and as such well suited to characterise the morphology of Ni-Mo nanoparticles. In this section, a brief overview of the working principle of and common artifacts in electron microscopy is given.

#### 3.4.1. Principles of TEM

In any form of microscopy, the resolution is by the wavelength of the radiation used; the shorter the wavelength, the better the possible resolution. In visible-light optical microscopy, this limits the point-to-point resolution to ca 200 nm [74], which is clearly too poor resolution to study most nanostructures. To circumvent this limitation and achieve, in the best case, atomic-scale resolution, in TEM, the incident radiation consists of electrons accelerated to high speeds by an applied voltage in the range of hundreds of kV. This gives a de Broeglie wavelength on the order of pm [75]. However, resolution is today limited not by the wavelength of the incident electron radiation, but by imperfections in the electromagnetic lens system used to focus the electron beam, discussed in more detail below; good microscopes can achieve resolution on the order of Å [75].

Two main modes of imaging can be distinguished: conventional TEM (sometimes called CTEM, but often simply TEM) and scanning TEM (STEM). In CTEM, the electron beam is focused by the lens system to be, ideally, parallel when hitting the specimen. This produces an image much in the same way as visible-light microscope: the entire specimen is illuminated and imaged at once. In contrast, in STEM, the beam is focused to a small spot, with size typically on the order of a nanometre, and scanned across the sample pixel-by-pixel, forming an image .

When the electron beam hits the sample, the electron can be scattered elastically or inelastically (i.e., with or without a loss of energy). Generally speaking, elastic interactions are the most important for imaging, as they are responsible for generating (useful) contrast. Inelastic scattering via collision with specimen electrons, on the other hand, can give valuable compositional information: if a beam electron interacts with a core electron of the sample, so that the core electron is promoted to between the Fermi and vacuum level, the amount of energy deposited is characteristic of the element in question. The spectrum of electron energy loss can be measured directly through electron energy loss spectroscopy or EELS. However, the interaction described previously also leaves the sample atom in an excited state, with a hole at the core levels. This excited state can be relaxed by demoting a higher-shell electron to the hole. The excess energy is released as characteristic X-ray radiation, which can be used to characterise the elemental composition of the sample through X-ray energy dispersive spectroscopy (XEDS). By performing STEM-XEDS, i.e., sampling the X-ray spectrum in each pixel of a STEM image, variations in composition throughout the sample can be mapped [76].

Several different wavelengths of characteristic radiation are usually possible for any given element. The characteristic peaks of an element are grouped into families: K, L, and M, depending on the shell in which the initial electron deficiency is generated. Since the generation of a characteristic X-ray requires core electrons of higher energy than the hole, it

follows that only elements with M-shell electrons can generate L peaks, while only elements with N-shell electrons can generate M peaks [76].

### 3.4.2. Artifacts in TEM

The wave nature of electrons means that many of the aberrations and artifacts germane to visible-light imaging also applies to electron imaging. In particular, for CTEM, resolution is limited by chromatic, and for older TEM spherical, aberration in the electron lenses, caused by the lens having different focal lengths for electrons of different wavelength or entering the lens near the middle or edge of the lens, respectively. Astigmatism, or radial asymmetry in the focussing power of the electron lens, distorts the dimensions of images. In crystalline structures, mismatch in overlapping planes give rise to Moiré fringes, or periodic contrast caused by the double diffraction of electrons through two sets of misaligned planes [77].

For XEDS, artifacts arise mainly from X-rays originating from other parts of the experimental system than the part of the sample under consideration, with different terminology depending on the source of the X-ray: spurious X-rays, system peaks, sum peaks, escape peaks and internal fluorescence [78].

Spurious X-rays arise from parts of the sample that are not illuminated directly by the sample, either due to scattering of the electron beam in the sample with subsequent excitation of X-rays, or through atoms absorbing part of an emitted X-ray's energy and re-emitting the energy as their own characteristic generation, so-called secondary fluorescence. System peaks arise by the same mechanism, but originate from the materials of the experimental system; e.g., any spectrum recorded on a copper grid will have a fairly strong copper signal independent of the sample. Sum peaks, escape peaks and internal fluorescence, finally, are features of the detector system, which is usually a Si-based diode that converts absorbed X-ray energy to current. Sum peaks arise from two X-rays hitting the detector simultaneously, causing the detector to register an X-ray at the sum of their energies. Escape peaks occur through the Si of detector (or more generally the detector material) absorbing and fluorescing some of an incident X-ray's energy, causing the detector to "see" an X-ray with an energy of  $E = E_{initial} - E_{Si K\alpha}$ . The X-ray fluoresced by the detector Si may in turn also be detected; this source of error is known as internal fluorescence [78].

## 4. Methods

### 4.1. Sample synthesis and preparation

Ni-Mo nanoparticles were synthesized via spark discharge generation. The details of the set-up have been described previously [17, 79]; however, a schematic overview of the setup is shown in Figure 3. For the capacitor electrodes, 3 mm wide Ni and Ni<sub>30</sub>Mo<sub>70</sub> rods were used, respectively. To prevent the formation of oxides, 5% H<sub>2</sub> in N<sub>2</sub> was used as a carrier gas. Compaction of the particles was carried out at 1200 °C, followed by deposition onto the substrate. The voltage across the capacitor was generally kept between 2.5 and 2.8 kV by adjusting the gap between electrodes as needed, keeping their separation at 1.5 mm. However, for the last batch of samples prepared, the small amount of electrode material left necessitated a shorter electrode gap and thus lower capacitor voltage, around 1.5 kV.

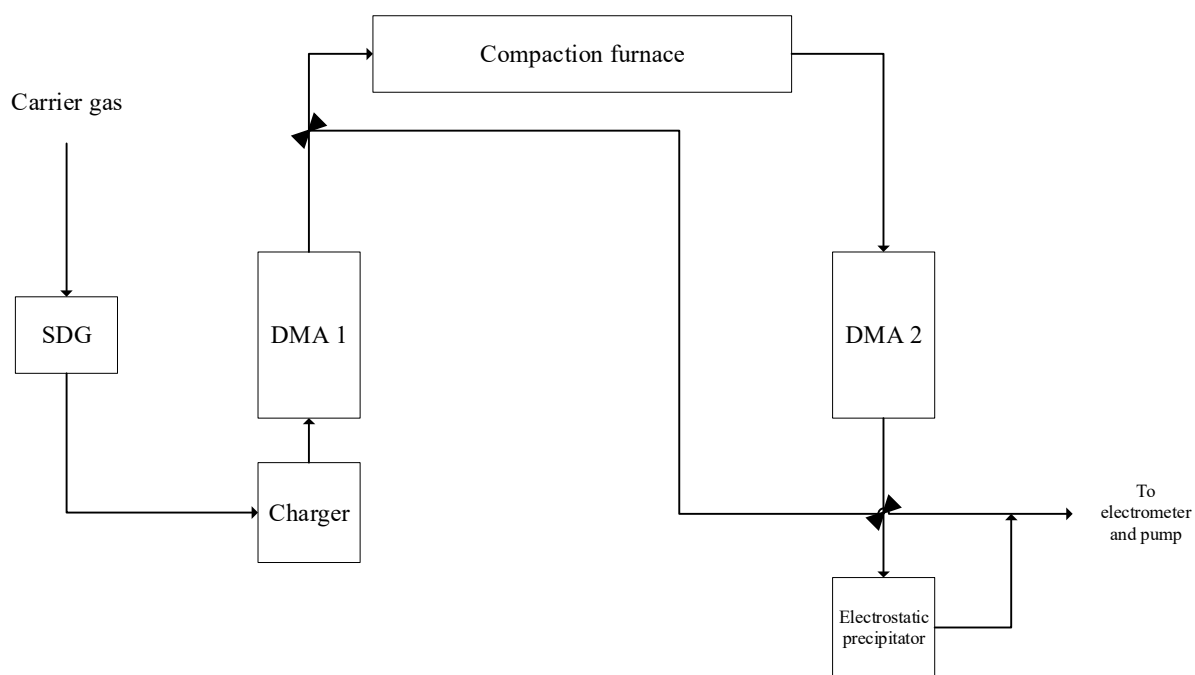


Figure 3: A schematic diagram over the SDG setup.

For PXRD samples, particles were after compaction deposited on 4x4 or 5x5 mm SiO<sub>x</sub> wafers (Siegert Wafer, J12004, lot nr. 317559) without size selection (i.e., bypassing both DMA's) to improve the deposition rate, with a target surface concentration of 7000 μm<sup>-2</sup>. The voltage across the capacitor was kept between 2.5 and 2.8 kV by adjusting the gap between electrodes as needed, keeping their separation at 1.5 mm. The target deposited surface concentration was set to 7000 μm<sup>-2</sup>.

Two types of TEM samples were prepared, size-selected and “bulk”. For size selected samples, particles were size selected for a mobility diameter of 25 nm after compaction using DMA2 (see [79]) and deposited onto 15 nm silicon nitride membrane grids (PELCO Prod. No. 21569CL-10, Batch CLEM-ULS-SN-MOS-A010(9)-T200-015\_BL22). The target

surface concentration was set to  $90 \mu\text{m}^{-2}$ . For “bulk” samples, particles were transferred onto lacey carbon Cu grids by gently moving the grids across the surface of a PXRD sample.

#### **4.2. Oxidation of particles**

The as-deposited nanoparticles were oxidised in air at 400, 510 and 600 °C. For size-selected samples, a 5 °C/min onramp was used, followed by holding for 5 min at the target temperature and a 15 °C/min offramp. The same programme was used for the bulk samples that were held for 5 min at the target temperature; for longer oxidation times, a 1 °C/min onramp was used.

For oxidation for 4 h at 400 and 510 °C, two samples with lower particle surface density were subjected to each treatment, and used together to improve the PXRD signal.

#### **4.3. Reduction of particles**

Reduction was carried out on size-selected samples previously oxidised at 400 °C in an atmosphere of 5% H<sub>2</sub> in N<sub>2</sub>. The temperature was ramped at 10 °C/min from room temperature, followed by holding at the target temperature (400 or 710 °C) for 2 h, finishing with a 15 °C/min offramp to room temperature.

To ensure the integrity of the SiN grids, the grids were loaded into an in-house holder consisting of a coiled copper wire suspending a sheet of aluminium foil, onto which the grids were loaded.

#### **4.4. PXRD**

Powder X-ray diffraction was carried out in transmission mode on the samples using a STOE STADI MP X-ray diffractometer equipped with a MYTHEN Dectrix 1k detector and using Cu K radiation. To make transmission possible, the samples were partially transferred from Si wafers to scotch tape, the latter of which was then loaded into the diffraction set-up.

Background subtraction and noise reduction was carried out using Profex 5.0.1 [80]. Reference spectra were obtained from ICSD (FIZ Karlsruhe) [81]. Structure indexation and refinement were carried out using DICVOL06 and Jana2006 [82].

#### **4.5. Ex situ CTEM and STEM study**

Imaging was carried out in a JEOL 3000F TEM at 300 kV accelerating voltage. XEDS spectra were acquired using an Oxford Instruments X-max 80 mm<sup>2</sup> detector.

Quantification of XEDS spectra and maps was carried out using INCA (Oxford Instruments) and the HyperSpy Python module. The variation in the atomic percentage was approximated using Gauss’s approximation formula (see Appendix B) using weight percentage error estimates extracted from INCA.

## 5. Results

### 5.1 General

Whenever the atomic percentage of Mo or Ni is referred to in the following text, unless otherwise stated, it is to be understood as a percentage of the sum of Ni and Mo. That is, “60 at. %  $\pm$  2 % Mo” is to be understood as a Ni:Mo ratio of between 42:58 and 38:62.

XEDS quantification results for the individual particles discussed throughout section 5 can be found in Table 3.

*Table 3: Atomic percentages of Mo in different particles with 95 % confidence intervals. As quantification of light elements such as oxygen is generally problematic in XEDS, the weight percentages rather than atomic percentages of oxygen are presented, without confidence intervals, in order to analyse the general trend; the numbers are not quantitatively correct. In all cases quantification is from INCA.*

Figure/Particle	History	Atomic percentage Mo		Weight percentage O
		Sum spectrum	Ni-Mo part	
Figure 9	As-deposited	75 % $\pm$ 2 %	64 % $\pm$ 2 %	-
Figure 10 (lower particle)	As-deposited	76 % $\pm$ 2 %	65 % $\pm$ 2 %	-
Figure 18a	Ox. @ 600 °C for 7h	55 $\pm$ 1 %	-	-
Figure 18b	Ox. @ 600 °C for 7h	56 $\pm$ 2 %	-	-
Figure 20	Ox. @ 400 °C for 5 min	60 % $\pm$ 1 %	-	38 %
Figure 21	Ox. @ 510 °C for 5 min	56 % $\pm$ 1 %	-	41 %
Figure 25	Red. @ 400 °C for 2 h	62 % $\pm$ 2 %	-	42 %
Figure 26	Red. @ 710 °C for 2 h	60 % $\pm$ 1 %	-	23 %
Figure 27	Red. @ 710 °C for 2 h	59 % $\pm$ 1 %	-	18 %

### 5.2. As-deposited nanoparticles

For a system containing 30 at% Ni and 70 at% Mo, the expected equilibrium composition is a two-phase system consisting of pure Mo combined with  $\delta$ -NiMo. For bulk as-deposited samples, Mo is clearly present, as indicated by the partially indexed PXRD pattern of non- in Figure 4. As shown in Figure 5-Figure 7, however, the additional peaks in the PXRD pattern do not match the theoretical  $\delta$ -NiMo patterns, nor do they agree with any other nickel-molybdenum intermetallic. Indeed, the peaks at 45.2° and 72.5 ° cannot be explained by any of the intermetallics, while all of the theoretical spectra indicate peaks that do not exist in the experimental data.

For as-deposited size-selected samples, the nanoparticles were mostly well-dispersed across the grid, as shown in Figure 8. Separation is typically on the order of 100 nm, although some

smaller clusters of 3-6 nanoparticles are present. Figure 8b showcases the typical Janus<sup>2</sup> morphology exhibited by these particles. Figure 9-14 show HRTEM images of the nanoparticles in Figure 8b, as well as XEDS maps of the same, while Figure 11 shows another Janus particle without XEDS map. The repeat distances exhibited by the Ni-Mo parts of the Janus particles can all be related to peaks in the PXRD spectra as shown in Figure 12, indicating that at least some, and likely all, of the unknown diffraction peaks correspond to the Ni-Mo part of the Janus particles.

Attempts at ab initio indexation of the unknown diffraction peaks using DICVOL06, however, yielded poor results. The best structure found, an orthorhombic structure with space group Pmmm (47),  $a = 9.3874$ ,  $b = 6.6383$ , and  $c = 3.1247$ , had a de Wolff FOM of 14.40, barely above the default minimum FOM of 10, and certainly not in the range of 20+ usually indicative of a good match [72]. The visual match of this structure with experimental data is also poor, giving peaks that are not observed, and failing to index others, as illustrated in Figure 13.

XEDS quantification of sum spectra corresponding to the particles in Figure 9-9 yields a total composition of ca 75 at.% Mo, which is somewhat above the original electrode percentage of 70 % (see Table 3). However, previous research indicates that while the experimental set-up yields an average Ni:Mo ratio of 30:70, there is significant local variation in the composition [83]. Furthermore, the quantification is not significantly different from that high-Mo regions observed in [83], and the result may thus be interpreted as being simply caused by sampling from a high-Mo region of the sample. In the Ni-Mo part of the nanoparticles (Table 3), the particles contain significantly more Ni, even when compared to the variation in [83], giving a ratio of ca 35:65. Like the diffraction peaks, this does not correspond to any known Ni-Mo intermetallic, further indicating that the diffraction peaks correspond to an unknown Ni-Mo phase.

Based on the above PXRD and TEM imaging evidence, it can be concluded that the as-deposited nanoparticles consist mainly of Janus particles, with one consisting of pure Mo and the other of an unknown Ni-Mo phase with a Ni:Mo ratio of around 35:65.

---

<sup>2</sup> A Janus particle is a biphasic particle with two distinct halves, each consisting of a single phase.

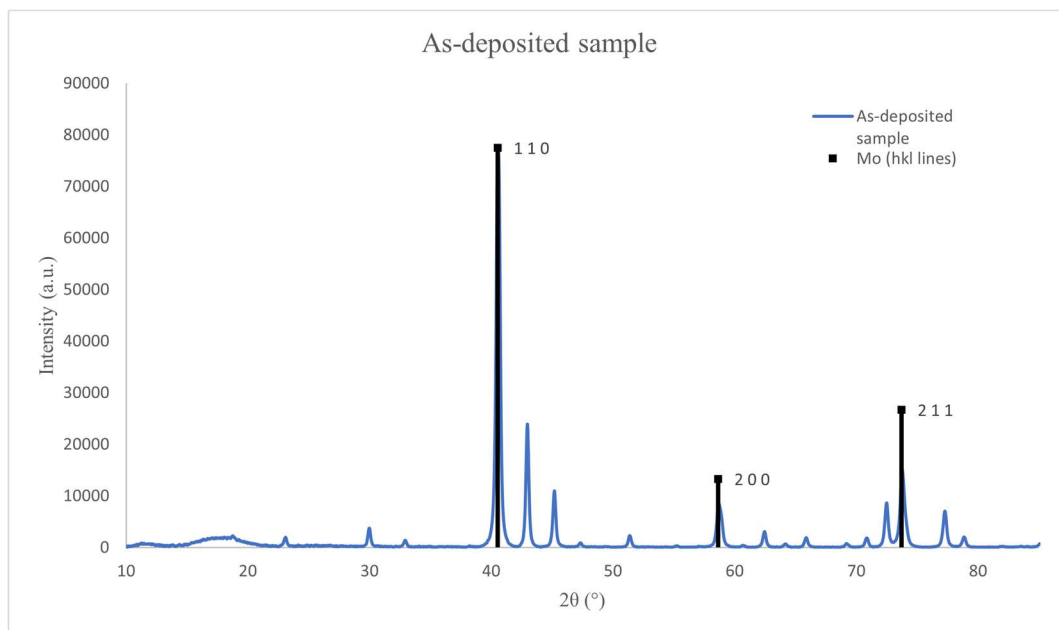


Figure 4: PXR D pattern of an as-deposited sample. The peaks corresponding to Mo have been indexed.

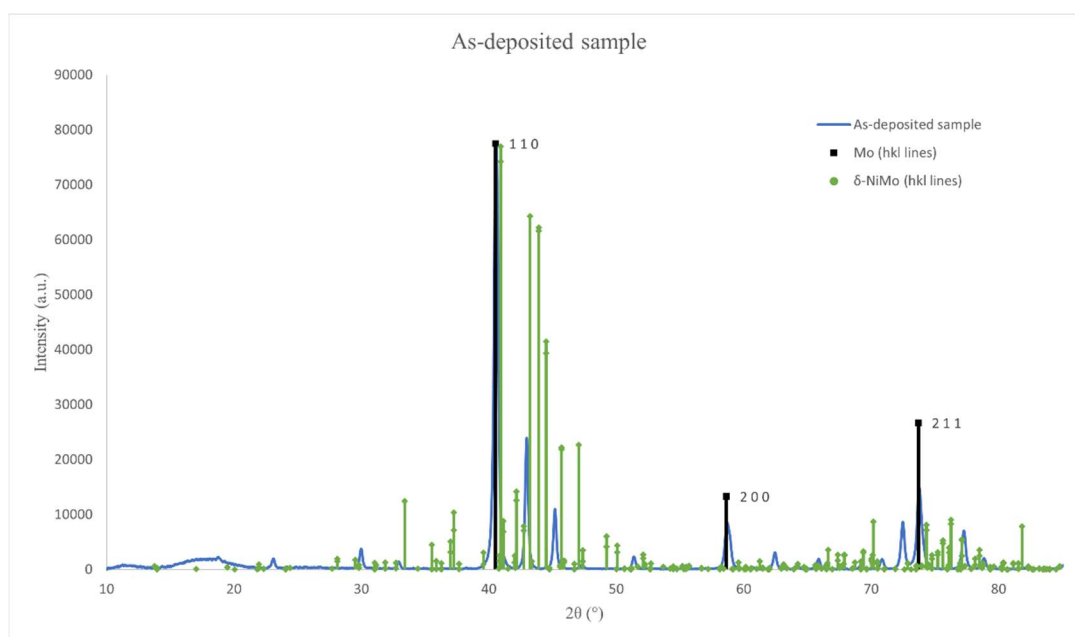


Figure 5: The PXR D pattern from Figure 4 with  $\delta$ -NiMo hkl lines for comparison. As can be seen, the  $\delta$ -NiMo lines cannot explain all the non-Mo lines, while some  $\delta$ -NiMo lines do not correspond to peaks in the pattern.

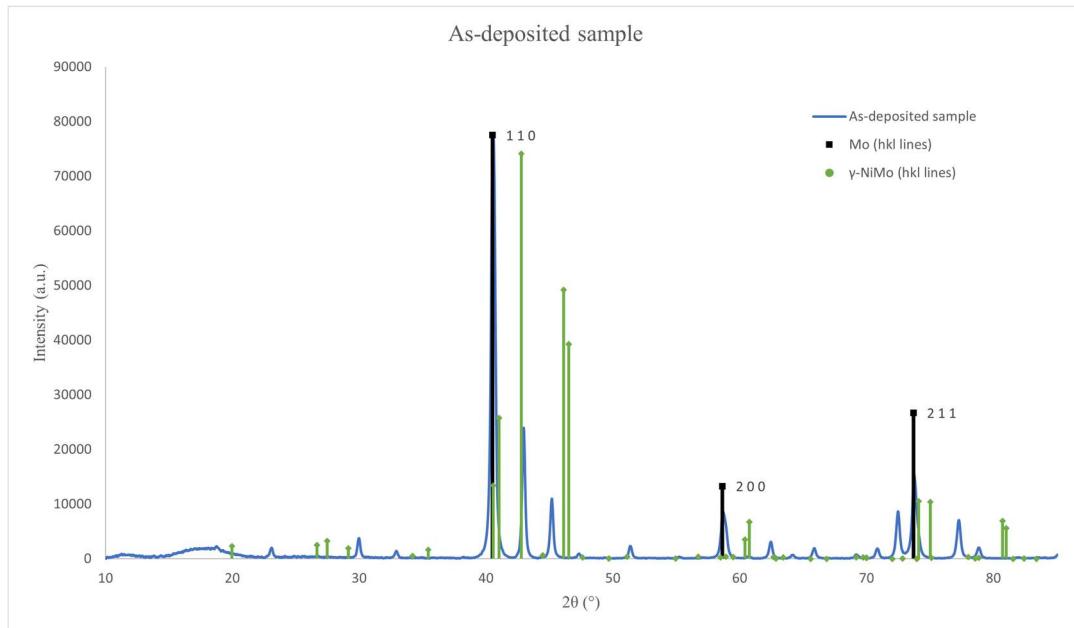


Figure 6: The PXR D pattern from Figure 4 with hkl lines for  $\gamma$ -NiMo. Just as for  $\delta$ -NiMo, the theoretical pattern fails to explain some peaks, and inserts peaks where there are none.

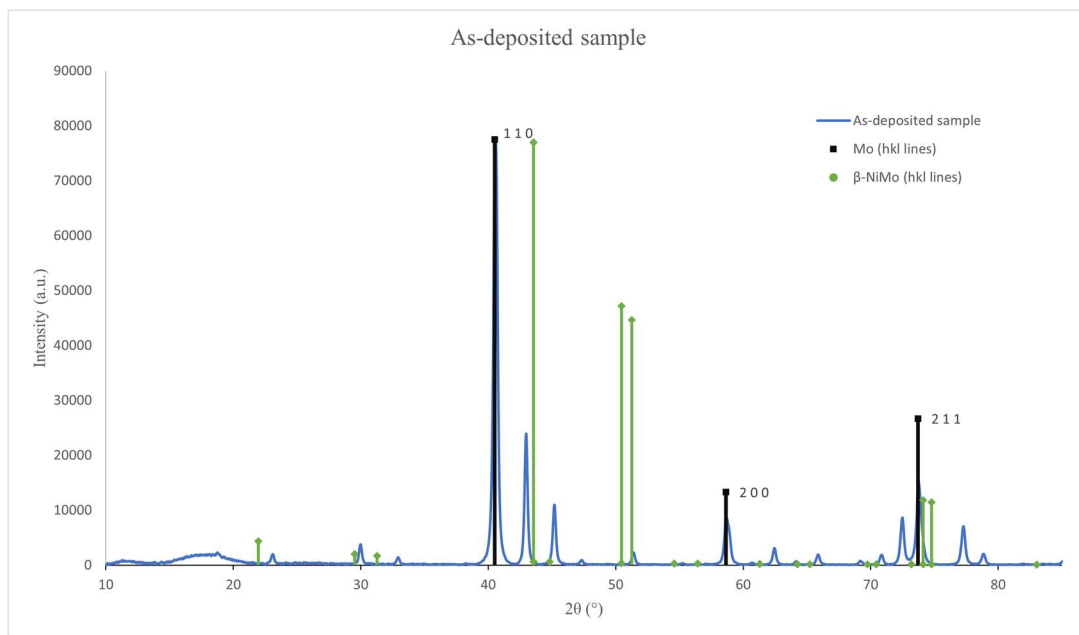


Figure 7: The PXR D diagram from Figure 4 with hkl lines for  $\beta$ -NiMo. Once again the match is poor.

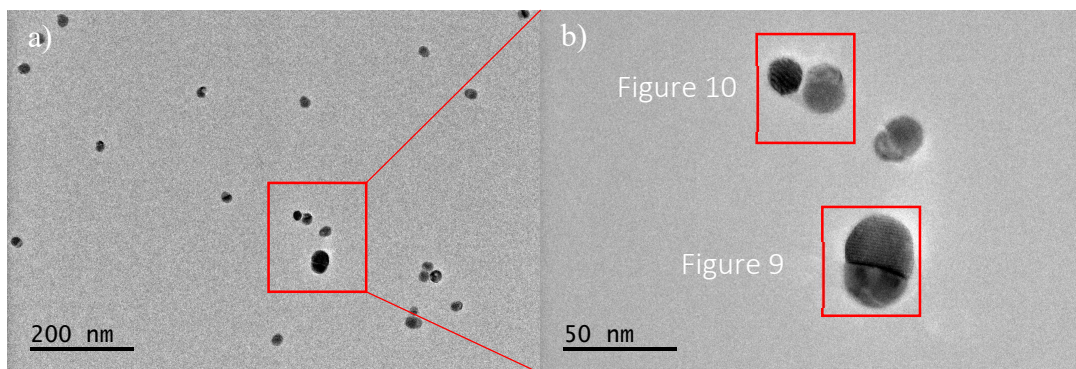


Figure 8: An overview of a size-selected as-deposited sample on an amorphous SiN grid. The Janus character of the particles can clearly be seen in b).

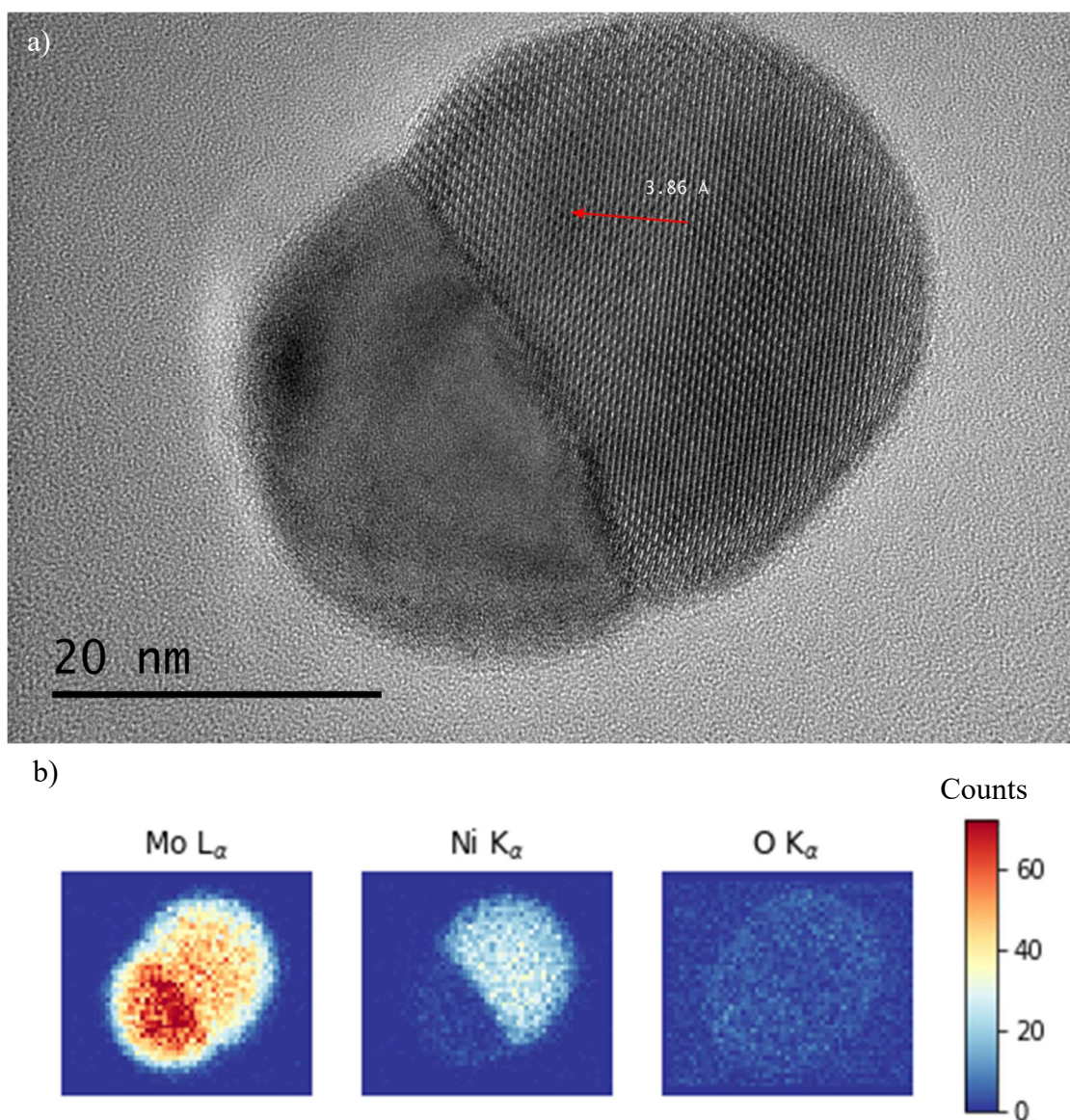


Figure 9: The larger Janus particle shown in Figure 8b. In a), a repeat distance of  $3.86 \text{ \AA}$  is showcased. In b), the particle can be seen to consist of an almost pure Mo part (lower half) and a mixed Ni-Mo part (upper half), with a small oxygen signal possibly indicating surface oxidation.

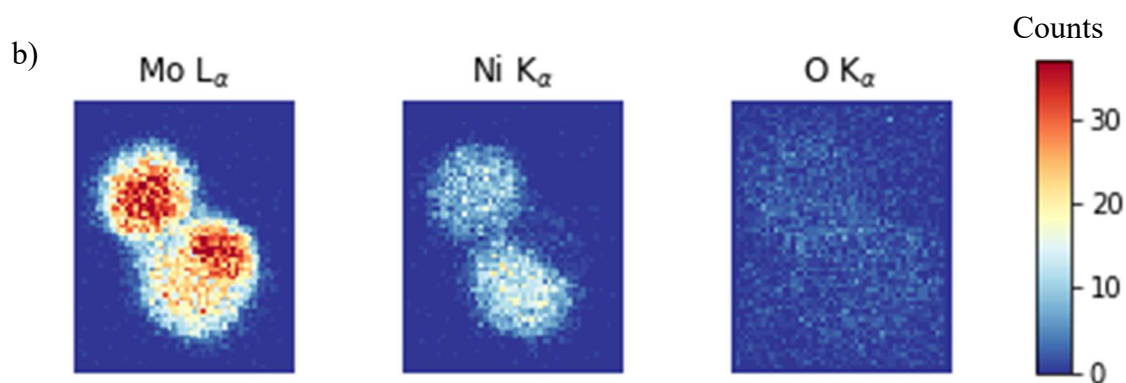
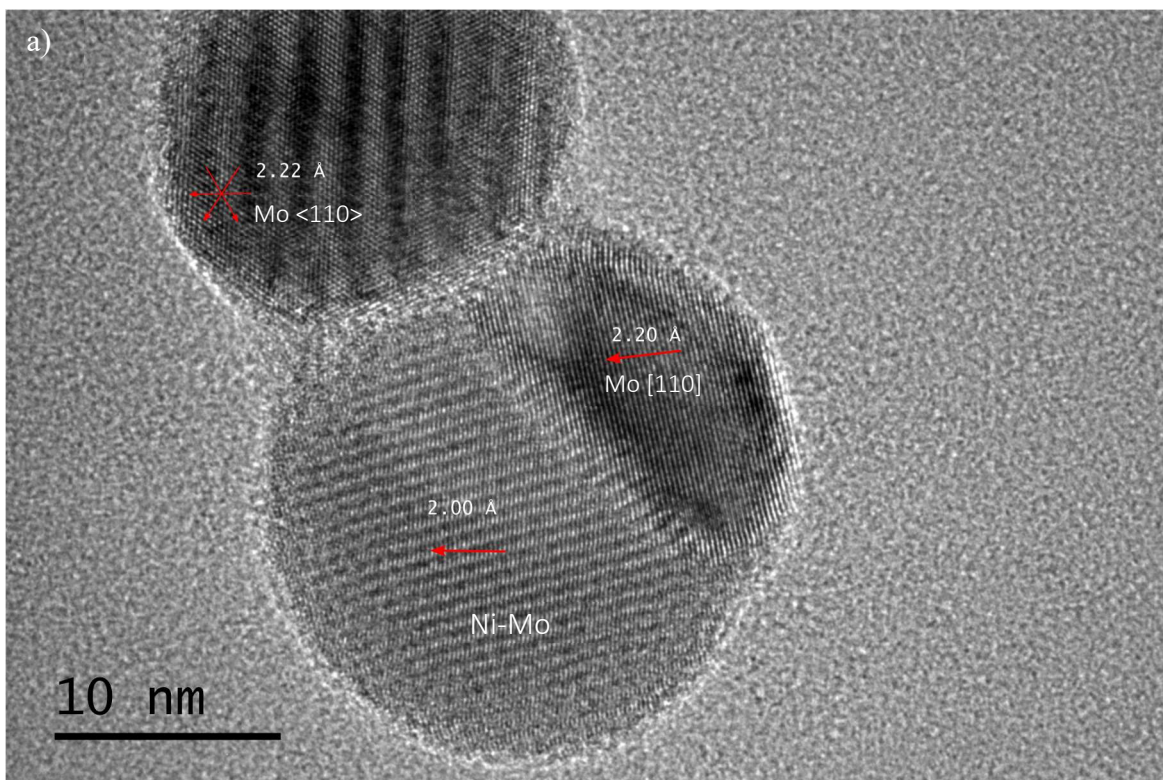


Figure 10: The smaller cluster of two nanoparticles from Figure 8. The indicated distances are periodicities in the indicated directions. In a), the repeat distances of the darker areas are within 1% of the Mo 110 interplanar distance, and the sixfold symmetry of the lattice in the upper particle indicates an orientation along the 111 direction. However, as can be seen in b), the upper particle is not pure Mo. This can be interpreted as the upper particle being a Janus particle protruding with its Mo end along the optical axis, which also explains the somewhat poor focus on each particle required to view all the indicated periodicities in the same image.

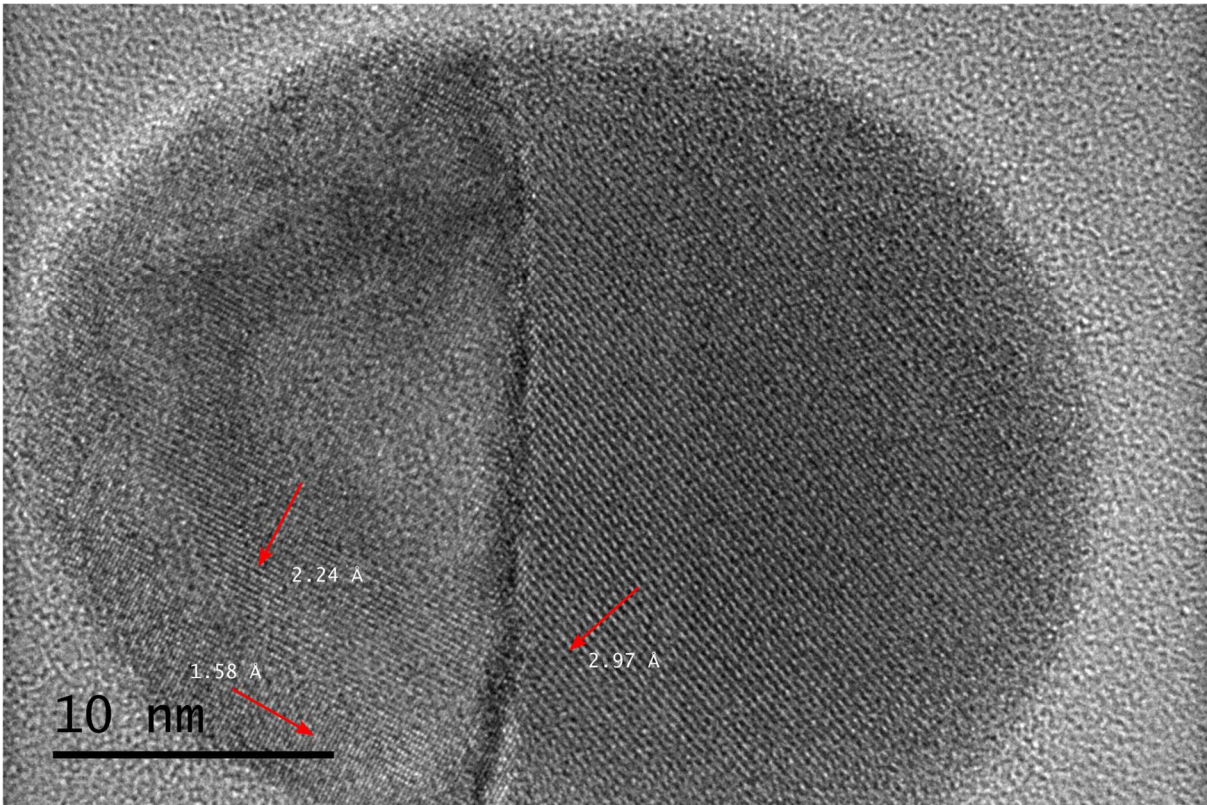


Figure 11: An additional Janus nanoparticle. The repeat distances indicated in the left half of the particle are within 1% of the Mo 110 (2.22 Å) and Mo 002 (1.57 Å) interplanar distances, allowing the repeat distance in the right half to be assigned to a Ni-Mo phase.

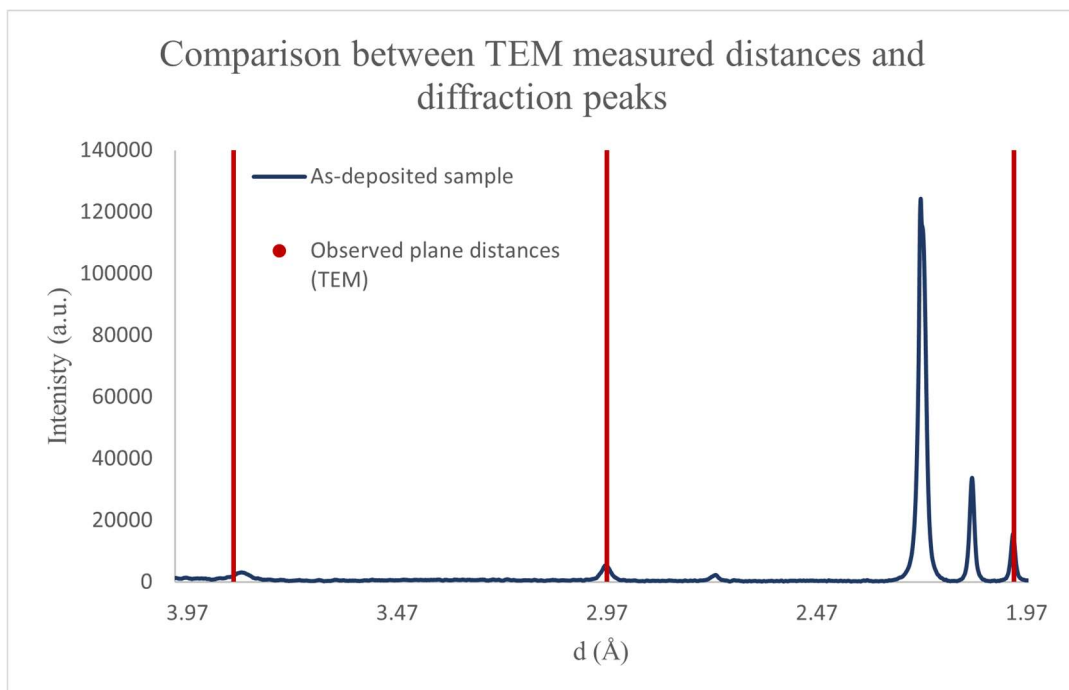


Figure 12: Comparison between the plane distances measured plane distances in Figure 9-15 and the diffraction pattern of the corresponding bulk sample limited to angular range of 22-47° and rescaled to interplanar distances.

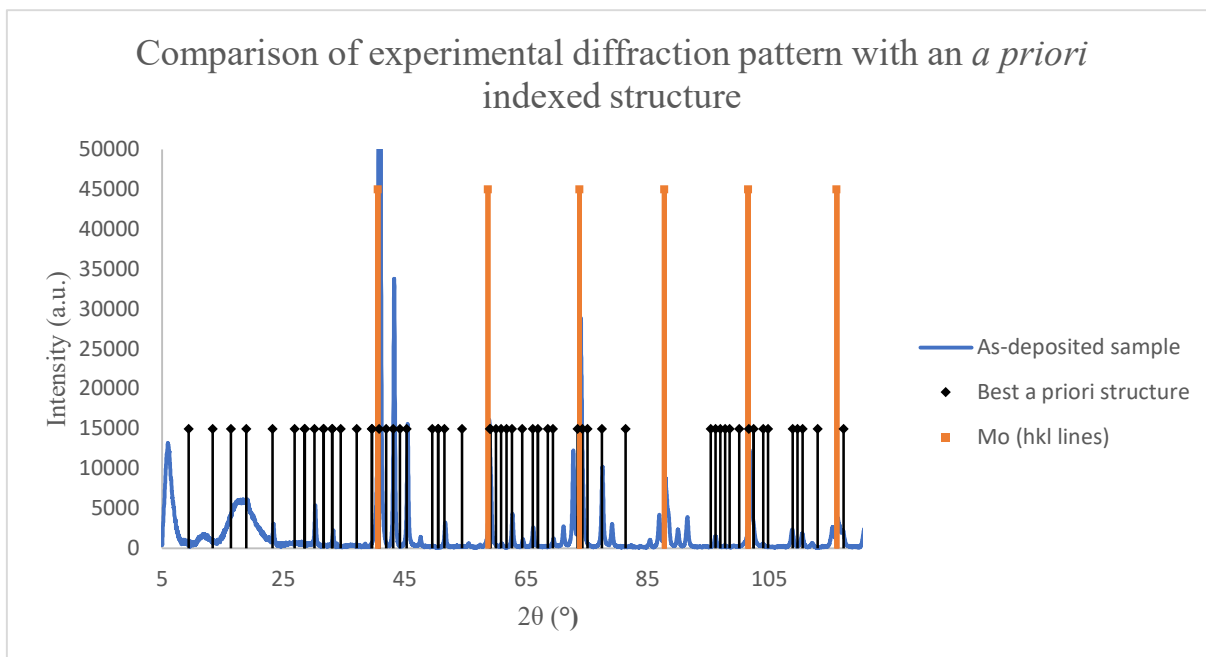


Figure 13: Comparison of a high-resolution PXRD pattern with the best *ab initio* structure found using DICVOL06, an orthorhombic structure with space group *Pmmm*. The structure has several peaks that do not exist in the pattern, and fails to index several peaks around 85°. The intense, broad peaks at low angles can be attributed to the scotch tape used as support.

## 5.2. Oxidised nanoparticles

For samples oxidised at 600 °C, the outcome is by and large the expected thermodynamically stable phases. However, as shown in Figure 14, initially, peaks indicative of  $\alpha$ - $\text{MoO}_3$ ,  $\alpha$ - $\text{NiMoO}_4$ , and the meta-stable  $\beta$ - $\text{NiMoO}_4$  can be seen, with the  $\beta$ - $\text{NiMoO}_4$  and  $\alpha$ - $\text{MoO}_3$  disappearing with increasing oxidation time.

PXRD on particles oxidised at 510 °C (Figure 15) and 400 °C (Figure 16) largely confirm this image, with an initial  $\beta$ - $\text{NiMoO}_4$  peak that disappears with time, while the intensity of the  $\alpha$ -signal increases. However, at 400 °C, the trend is less clear cut, with the relative intensity of the  $\beta$ - $\text{NiMoO}_4$  220 peak actually being higher after 4 h than after 1 h. Consistently throughout the PXRD spectra, but especially at 400 °C, the  $\beta$ - $\text{NiMoO}_4$  220 peak is also noticeably broader than other peaks, indicating a small domain size compared to the other phases present.

TEM imaging on particles oxidised at 600 °C further confirm the general picture painted by PXRD. Figure 17 shows a TEM image of a sample oxidised at 600 °C for 1 h, with large particles and periodicities indicative of  $\alpha$ - $\text{NiMoO}_4$ . Compositional determination with STEM-XEDS gives a Ni:Mo ratio of 49:51 and shows a uniform distribution of Ni and Mo in these crystallites (Figure 18).

For particles oxidised at lower temperatures, size-selected samples were made and characterised. Figure 19a and c show an overview of size-selected sample oxidised at 400 °C and 510 °C, respectively. Overall, the particles have remained dispersed during the oxidation treatment, with the larger and less round particles likely being attributable to the smaller clusters of nanoparticles observed in Figure 8. An example of a larger oxidised nanoparticle is shown in Figure 20, together with the corresponding XEDS map. The particle exhibits a notable “cauliflower” or “popcorn” structure, with a central void surrounded by smaller domains of oxide. The distribution of Ni and Mo is uniform, with a molybdenum content of 60 at. %  $\pm$  1 %. The hollow shape roughly matches the size of the as-deposited nanoparticles; as such, the formation can be referred to the Kirkendall effect, as previously observed in pure Ni nanoparticles. However, as shown in Figure 21, smaller nanoparticles also exist that do not exhibit a hollow core, with a slightly lower Mo content of 56 at. %  $\pm$  2 %. The smaller particle exhibits periodicities consistent with the (001) and (11 $\bar{1}$ ) planes of  $\beta$ - $\text{NiMoO}_4$ , whereas the observable periodicities in the larger particle are mostly consistent with both  $\alpha$ - $\text{NiMoO}_4$  and  $\beta$ - $\text{NiMoO}_4$ , although the plane distances around 3.33 Å only match the 220 planes of  $\beta$ - $\text{NiMoO}_4$ . The observation of  $\beta$ - $\text{NiMoO}_4$  in these smaller domains is consistent with the line broadening observed in PXRD.

Imaging of bulk samples at 400 °C further confirm the presence of small domains of  $\beta$ - $\text{NiMoO}_4$ . Figure 22 shows an image of the bulk sample oxidised for 5 min at 400 °C. The morphology seems to be multiple smaller crystalline domains sintered into larger clusters, part of which is possibly amorphous. Plane distance measurements indicate the presence of both  $\alpha$ - $\text{NiMoO}_4$  and  $\beta$ - $\text{NiMoO}_4$ , consistent with the results from Figure 16.

In conclusion, oxidation of the as-deposited nanoparticles appears to favour  $\beta$ - $\text{NiMoO}_4$  when the domain size is small, as when artificially constricted by the isolated nature of the size-selected nanoparticles, or when short time or low temperature has prevented sintering of the particles.

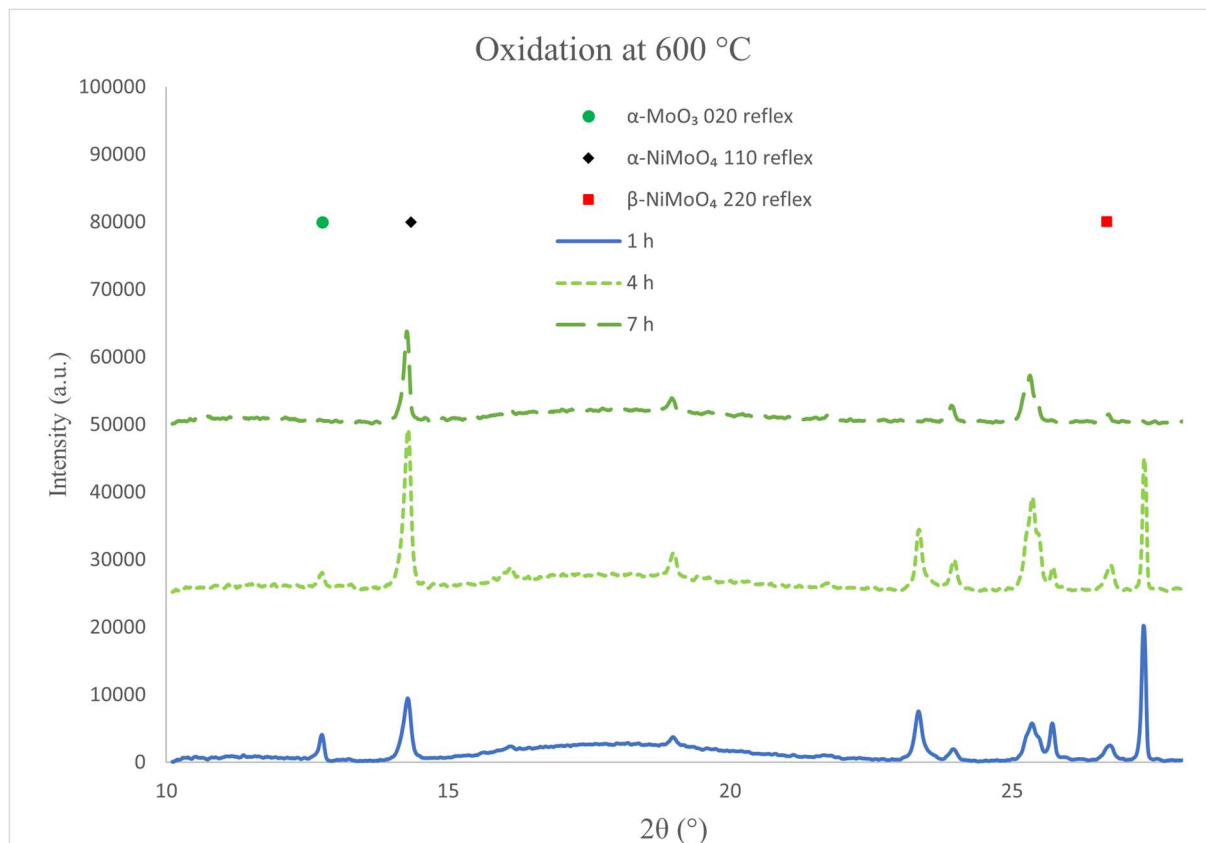


Figure 14: PXRD spectra for bulk samples oxidised at 600 °C, with selected non-overlapping peaks characteristic of  $\alpha$ - $\text{MoO}_3$ ,  $\alpha$ - $\text{NiMoO}_4$ , and  $\beta$ - $\text{NiMoO}_4$  marked as shown in the legend. The spectra have been arbitrarily offset and rescaled along the intensity axis for clarity.

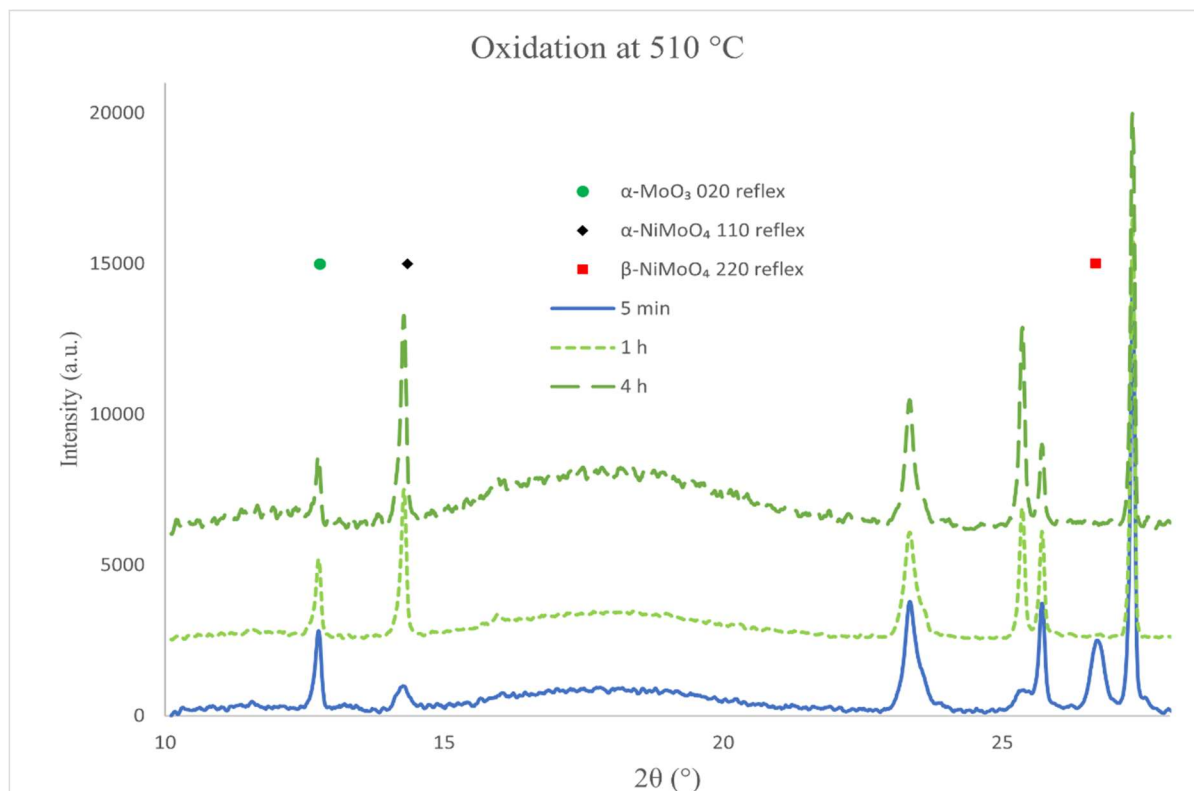


Figure 15: PXRD spectra of bulk samples oxidised at 510 °C, with selected non-overlapping peaks characteristic of  $\alpha$ - $\text{MoO}_3$ ,  $\alpha$ - $\text{NiMoO}_4$ , and  $\beta$ - $\text{NiMoO}_4$  marked as shown in the legend. The spectra have been arbitrarily offset and rescaled along the intensity axis for clarity.

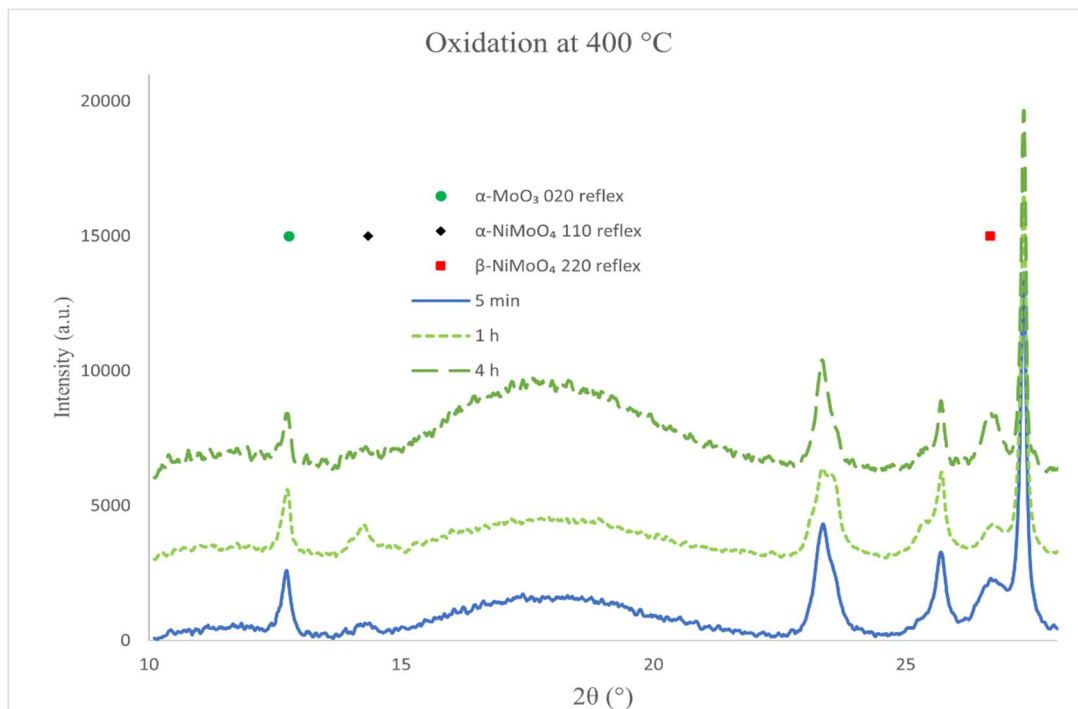


Figure 16: PXRD spectra for bulk samples oxidised at 400 °C, with selected non-overlapping peaks characteristic of  $\alpha$ - $\text{MoO}_3$ ,  $\alpha$ - $\text{NiMoO}_4$ , and  $\beta$ - $\text{NiMoO}_4$  marked as shown in the legend. The spectra have been arbitrarily offset and rescaled along the intensity axis for clarity.

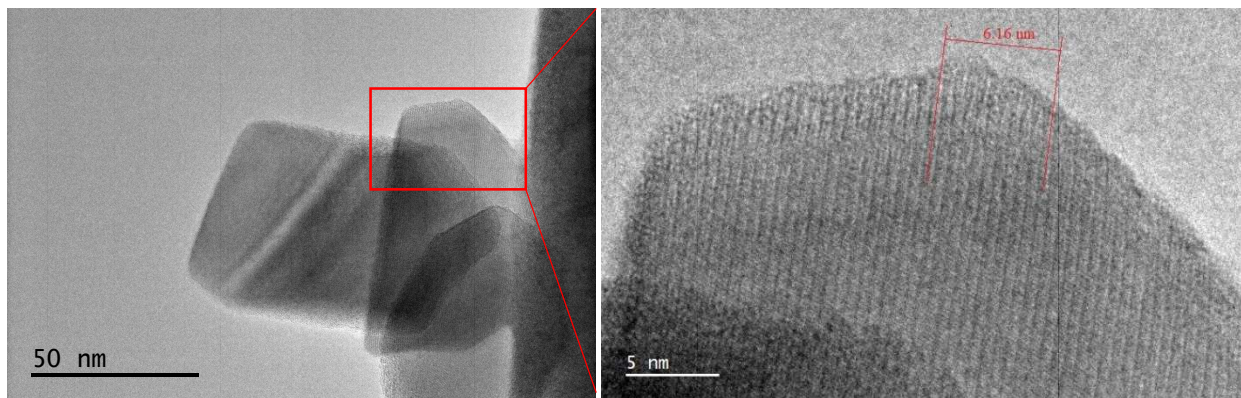


Figure 17: TEM image of smaller crystallites. In the inset, the indicated spacing covers 10 repeating units, and correspond in length to 10 110 planes in  $\alpha$ - $\text{NiMoO}_4$ .

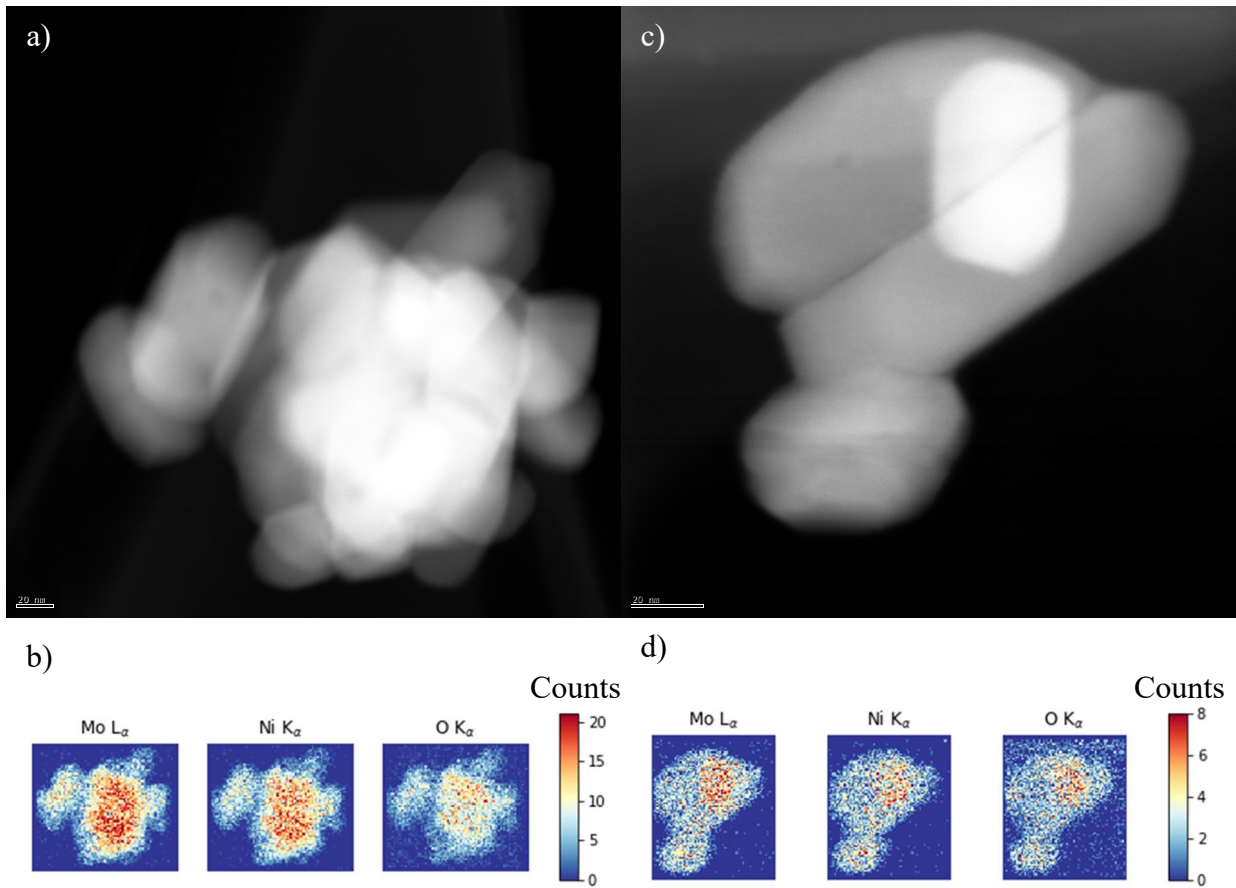


Figure 18: HAADF-STEM images of particle clusters in a sample oxidised for 1 h at 600 °C. In a and c, the scale bar signifies 20 nm.

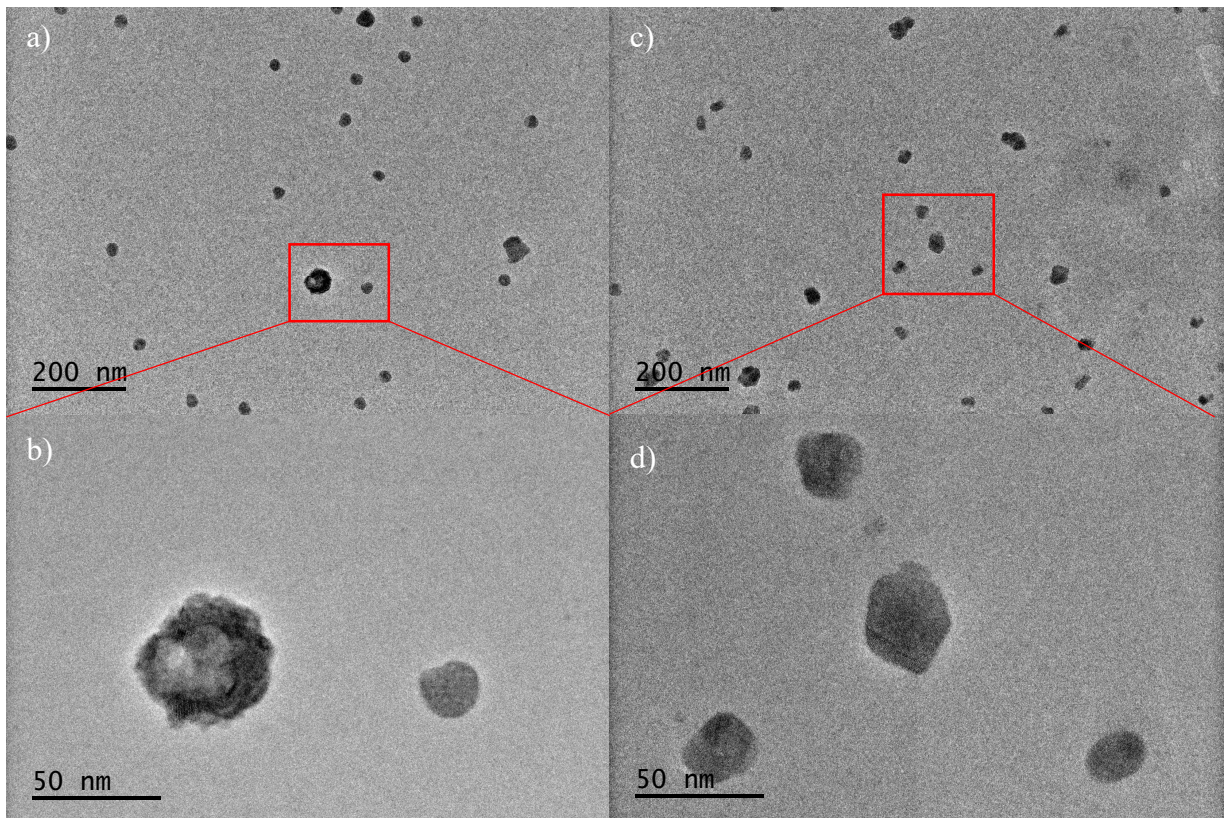


Figure 19: a) and b): Size-selected nanoparticles oxidised at 400 °C. c and d): Size selected particles oxidised at 510 °C.

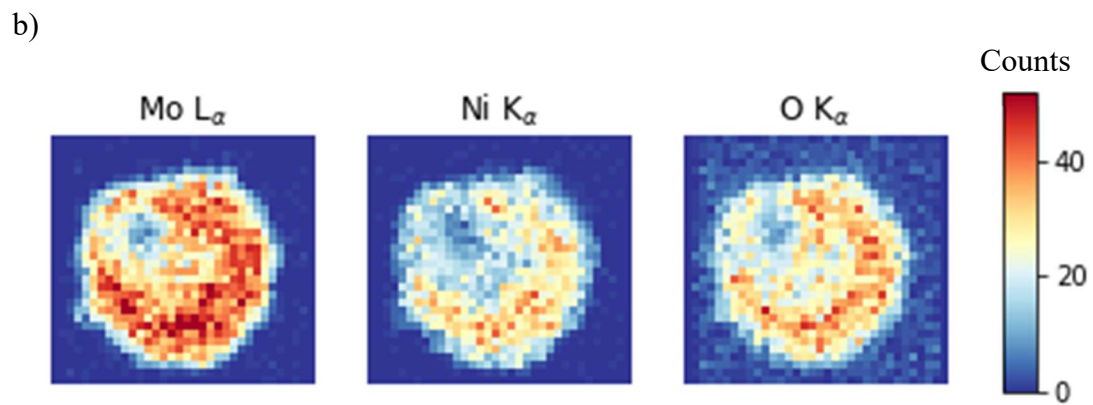
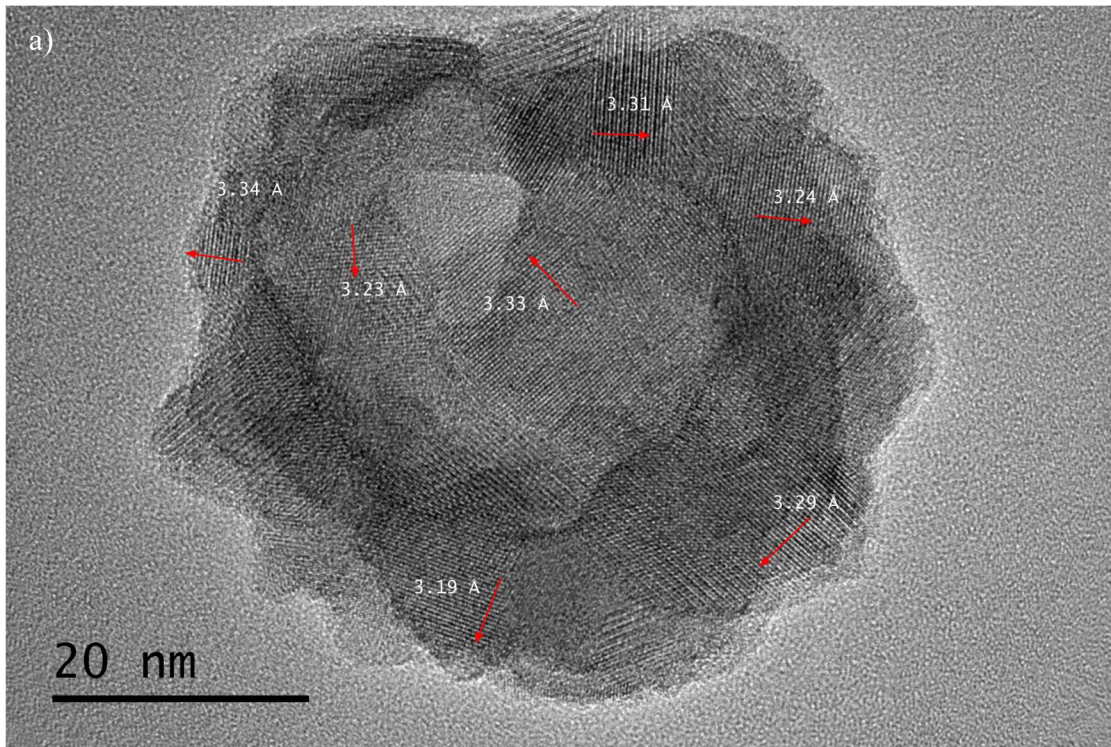


Figure 20: a) Close-up of the larger particle from Figure 19b. b) XEDS map of the same. A hollow can be seen in the upper left half of the particle in both images.

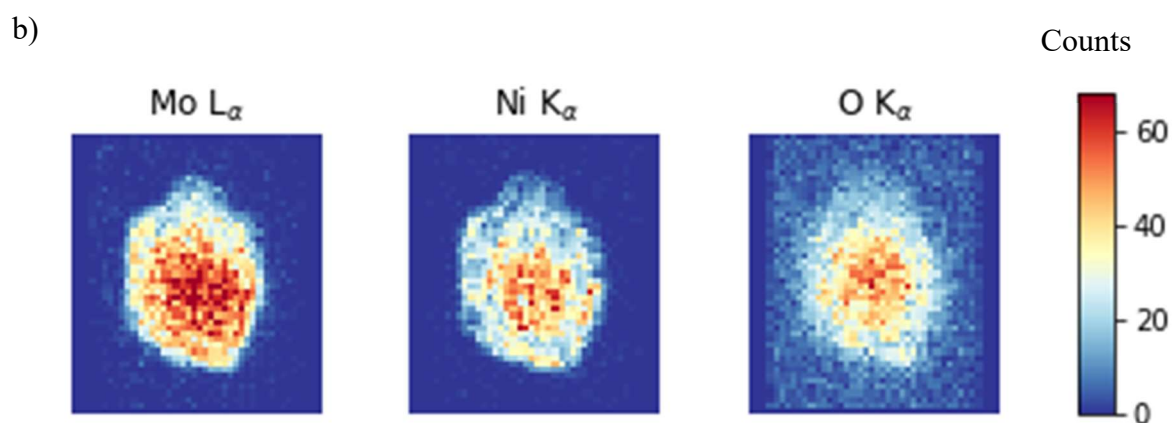
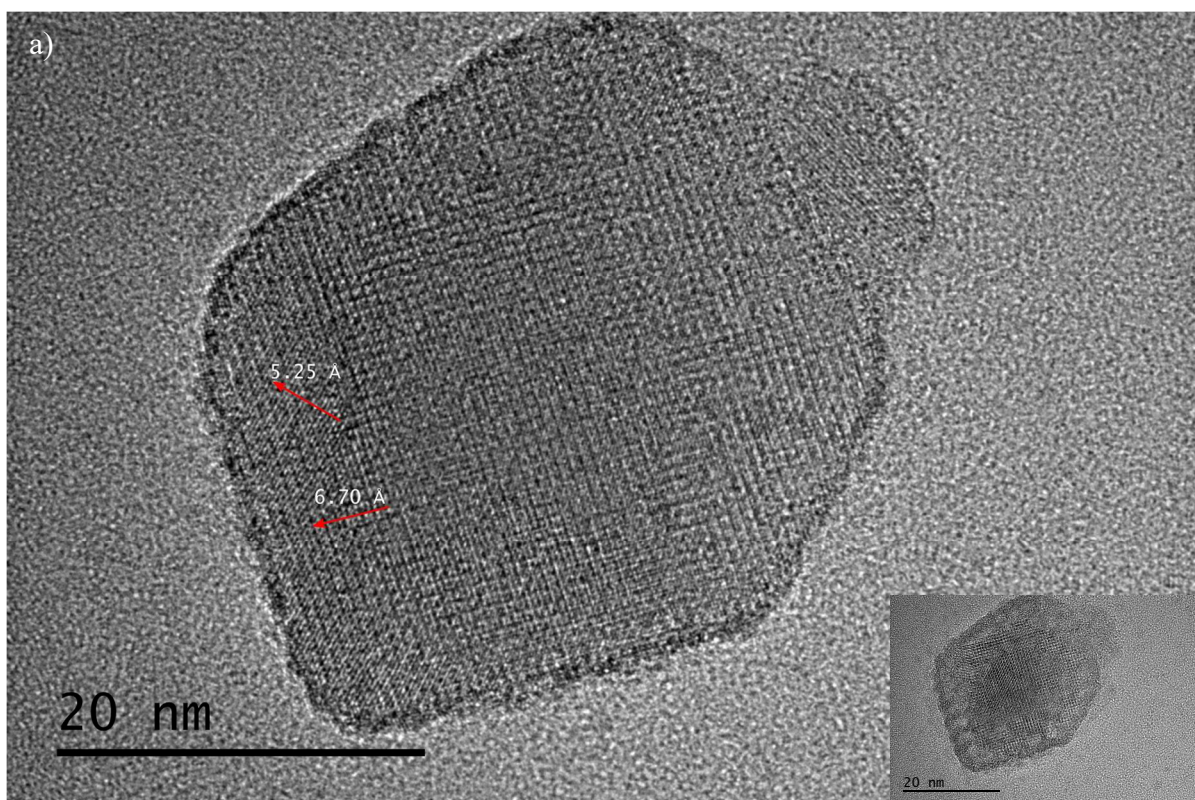


Figure 21: a) The central particle in Figure 19d, with periodicities corresponding to the (001) ( $6.68 \text{ \AA}$ ) and (11 $\bar{1}$ ) ( $5.29 \text{ \AA}$ ) planes of  $\beta\text{-NiMoO}_4$ . Inset: The same particle after a few minutes under the beam. Beam damage is evident around its edges. b) XEDS maps of the same particle. The “fringe” visible in the XEDS map can be attributed to beam damage as shown in the inset in a).

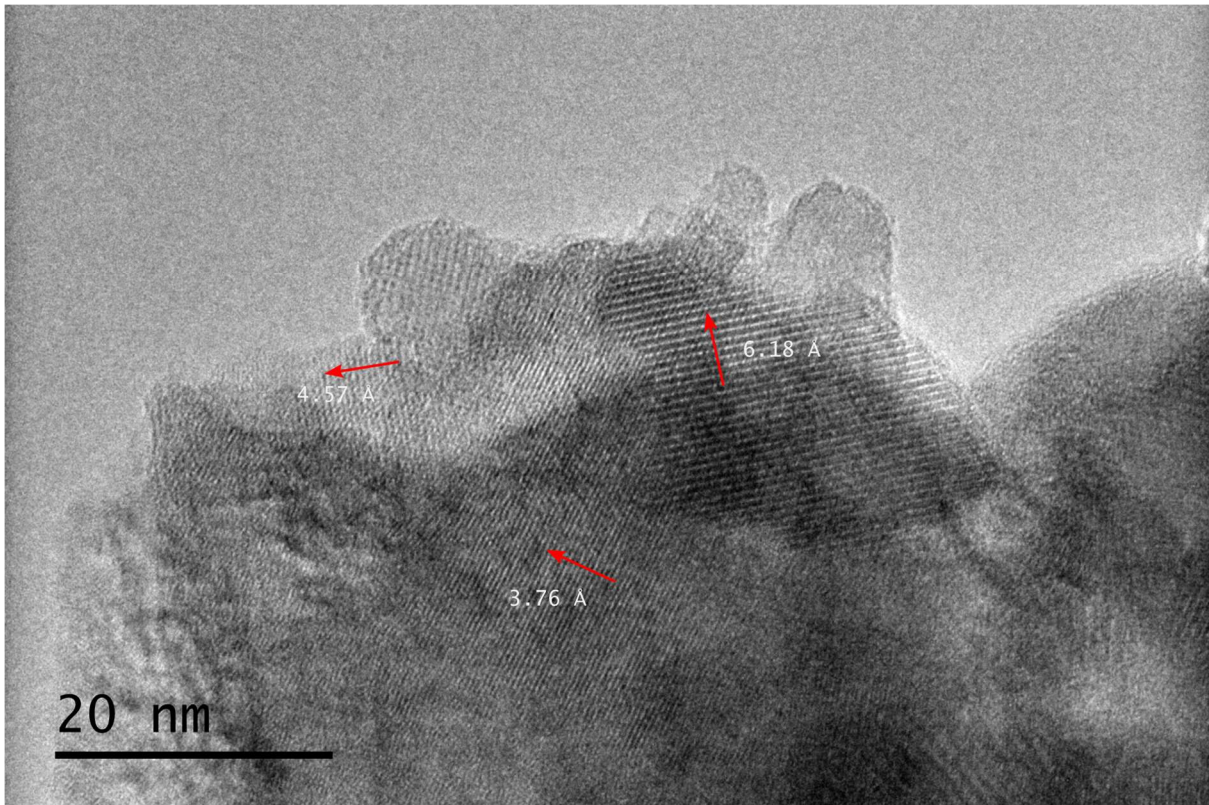


Figure 22: CTEM image of a bulk sample oxidised for 5 min at 400 °C. The distances are consistent with  $\alpha$ -NiMoO<sub>4</sub> 110 interplanar distances (6.17 Å),  $\alpha$ -NiMoO<sub>4</sub> 101 interplanar distances (4.60 Å), and  $\beta$ -NiMoO<sub>4</sub> 021 interplanar distances (3.79 Å).

### 5.3. Reduced nanoparticles

In general, the particles in size selected samples continued to be stable on the SiN grids, with minimal inter-site sintering being apparent. Figure 23 shows an overview of the sample reduced at 400 °C, where the particles can still be seen to be well-dispersed on the surface of the grid.

At a reduction temperature of 400 °C, little morphological change could be observed, as shown in Figure 24 and Figure 25. For example, in Figure 24, the same type of “cauliflower” structure as in Figure 20 is still evident, with repeat distances consistent with NiMoO<sub>4</sub>. The large, rounded part of the particle shown in Figure 25 appears to consist mainly of copper, and can be attributed to contamination from the set-up, which contains a spool of copper wire which came into contact with the sample briefly; otherwise, little morphological change appears to have occurred. The lack of obvious morphological change at this temperature is consistent with earlier TPR reports on mixed Ni-Mo oxides [13].

In contrast, at 710 °C, the particles change drastically, as shown in Figure 26 and Figure 27. Compared to Figure 24 and Figure 25, great morphological changes are apparent. The rather diffuse and “smeared” spots arranged in rings in the Fourier transform of Figure 26 and Figure 27 (shown in Figure 28) indicate that the particles consist of many small ordered domains, causing broadening of the “diffraction spots”. STEM-XEDS maps show segregation of the Ni and Mo compared to the uniform distribution observable in the oxidised particles, consistent with previous reports concerning reduction of NiMoO<sub>4</sub> nanorods [56]. The dark fringes visible at the edge of the particle in Figure 26a are at first glance reminiscent of the layered structure of MoS<sub>2</sub>, the presence of which would not be impossible, as the test tube used for reduction had a small unknown contamination which was not possible to remove.

However, due to pathological overlap of the Mo L<sub>α</sub> (2.293 keV) and S K<sub>α</sub> (2.308 keV) lines, the presence or absence of sulfur in the structure could not be confirmed. Furthermore, the repeat distance (6.59 Å) is not consistent with any plane spacings in the known ambient-pressure MoS<sub>2</sub> structures. Another possibility is that the fringes are Moiré fringes, judging by their long period. Their location along the edge of the crystal, and nowhere else, would in this case indicate that a structural change has occurred along the edge of crystal, for example a change from MoO<sub>3</sub> to MoO<sub>2</sub>, also as expected from previous TPR measurements [13]. The oxygen weight percentages in Table 3, although not reliable in their absolute value, further indicate a loss of oxygen compared to the oxidised particles and those reduced at 400 °C and oxidised particles, with those reduced at 400 °C not appearing to differ significantly in composition from non-reduced particles.

The above results indicate that the reduction of the nanoparticles by and large follow the trends observed for larger specimens of NiMoO<sub>4</sub> in previous literature. That is, in contrast to what is observed for the oxidation of the nanoparticles, no potential size effects or similar are apparent.

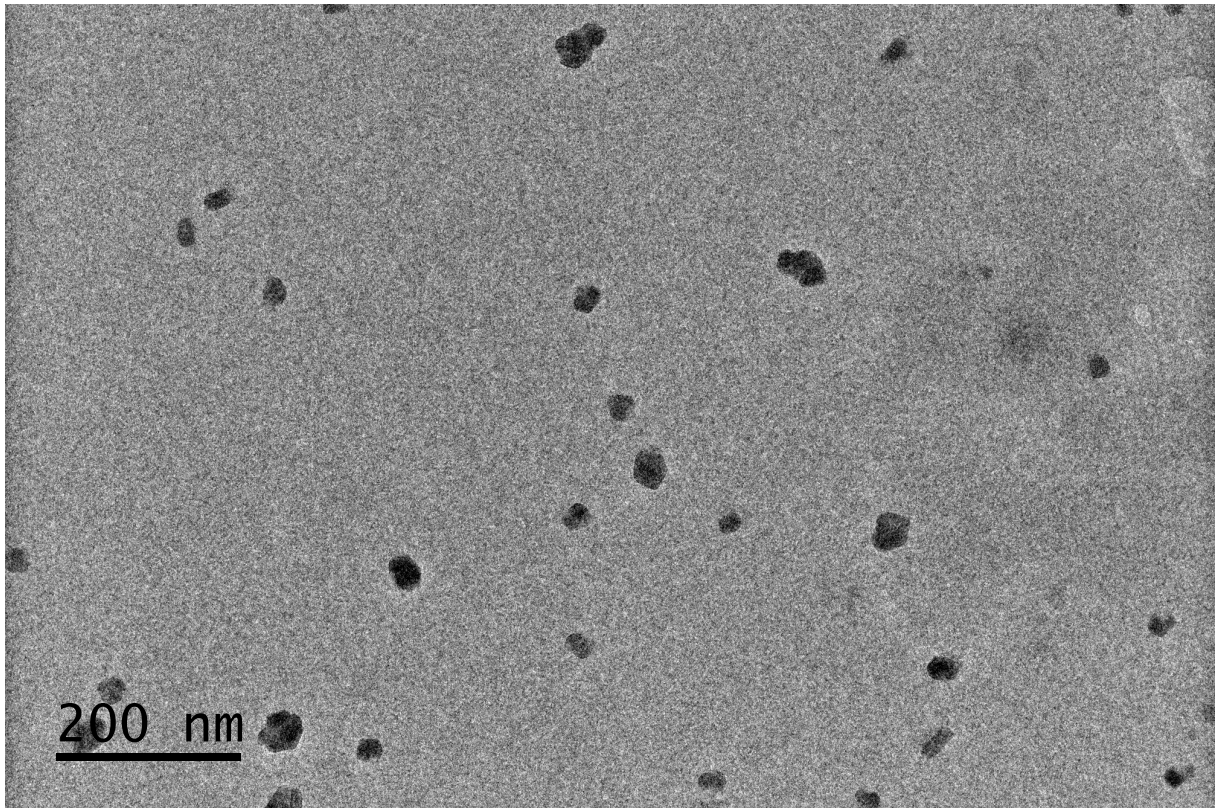


Figure 23: Overview of the sample reduced at 400 °C.

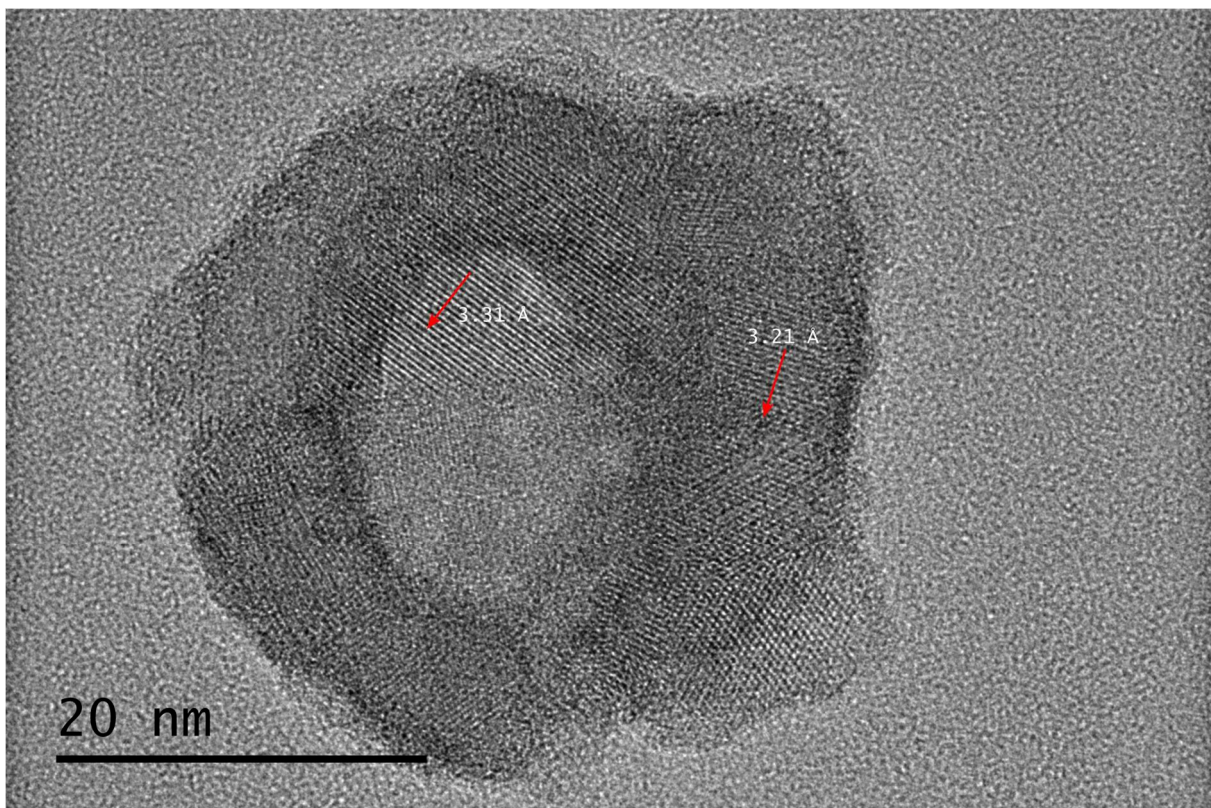


Figure 24: A "cauliflower" particle after reduction at 400 °C. The indicated plane spacings are consistent with  $\beta$ -NiMoO<sub>4</sub> 220 (3.33 Å) and  $\bar{2}02$  (3.23) plane spacings.

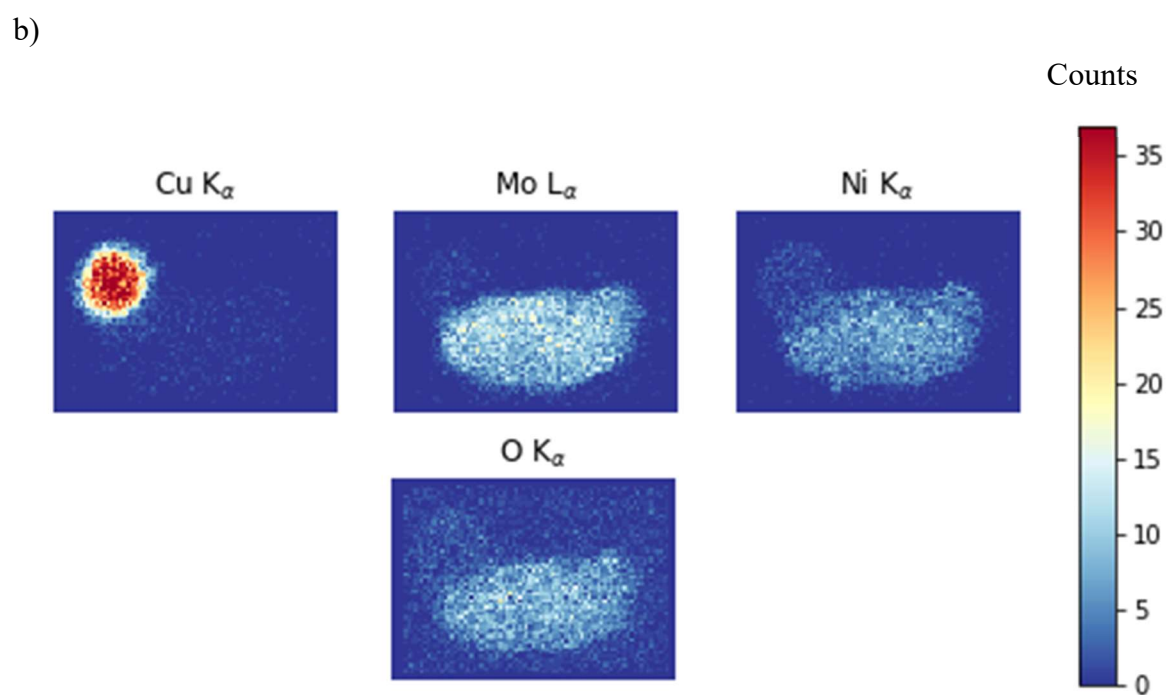
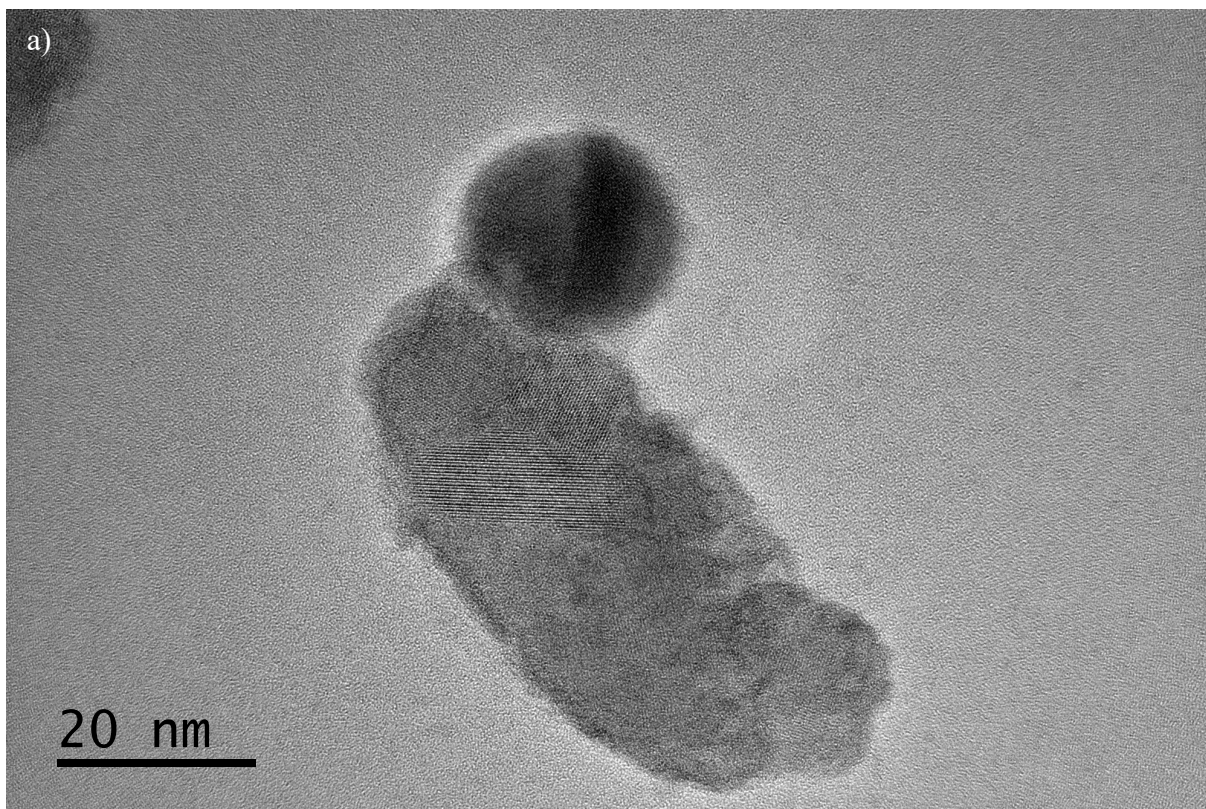


Figure 25: Smaller oblong particle with copper contamination. Plane spacings are consistent with both polymorphs of  $NiMoO_4$ .

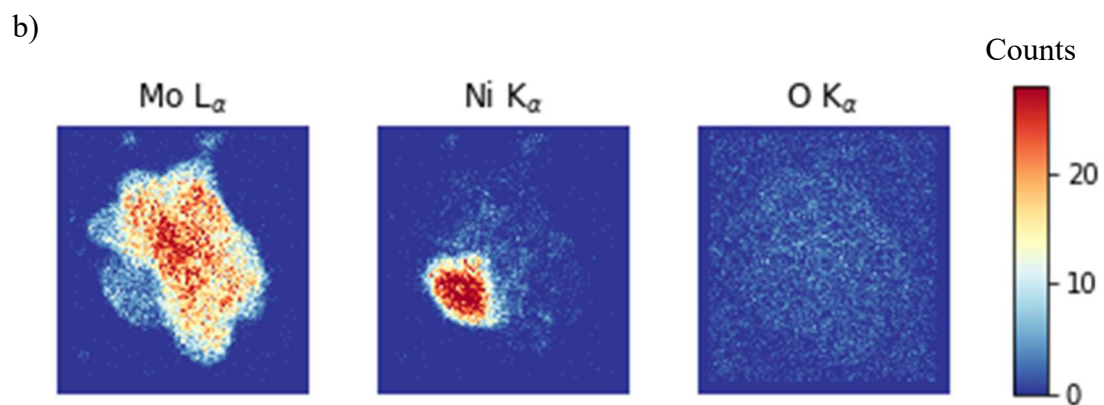
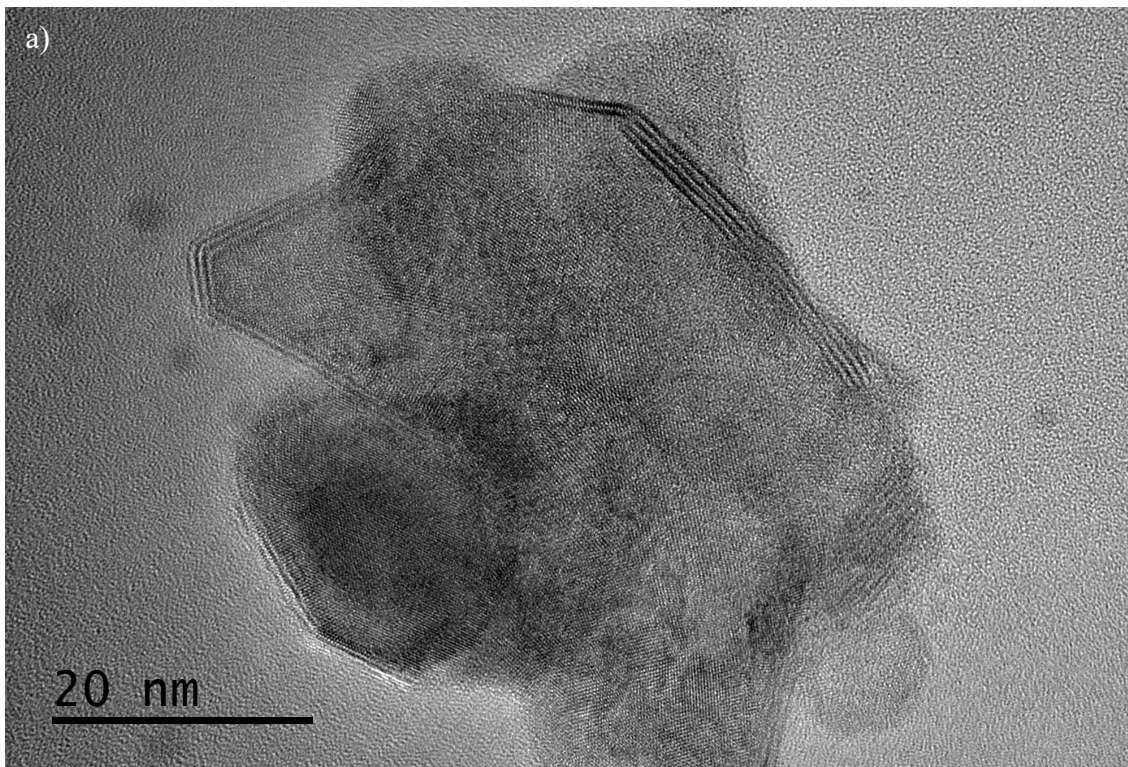


Figure 26: a) TEM image of a particle or particle cluster reduced at 710 °C. b) XEDS map of the same particle. The nickel can be seen to have clearly segregated from the rest of the material.

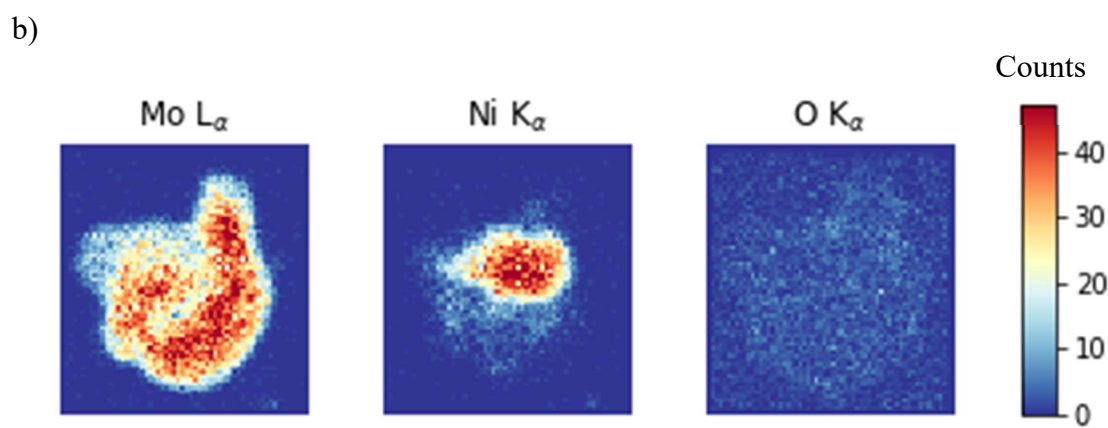
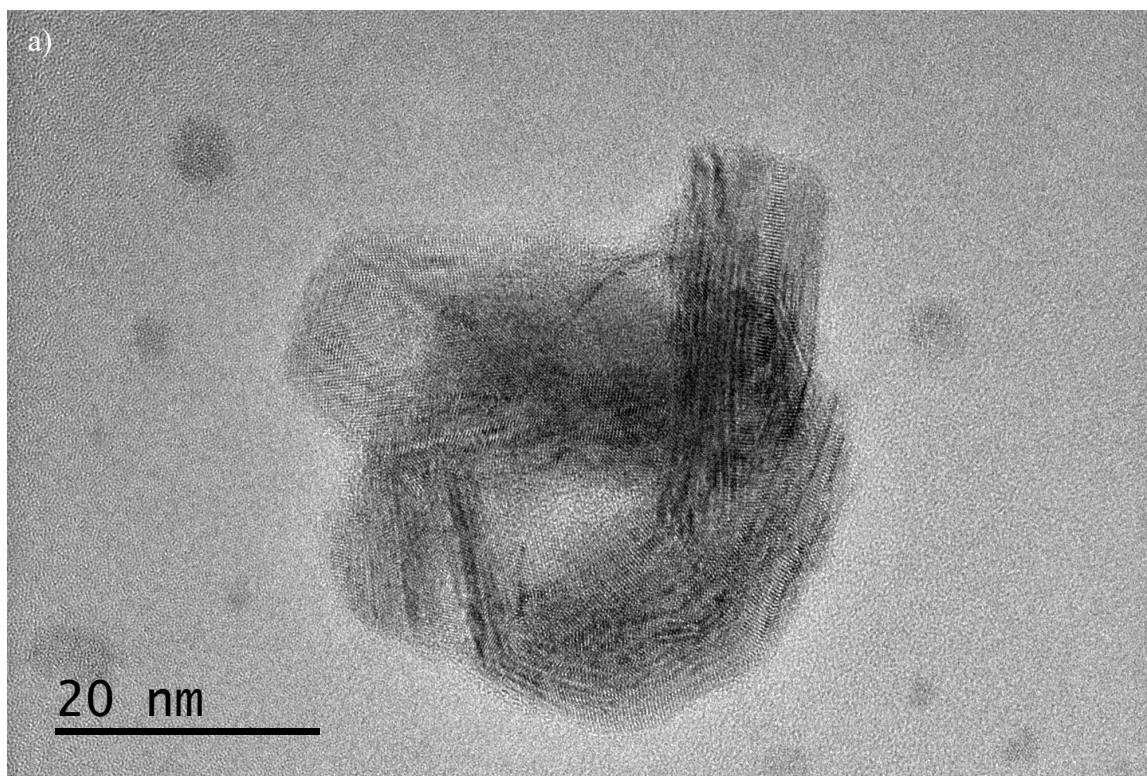


Figure 27: A particle reduced at 710 °C with a central void. a) TEM image. b) XEDS map. The nickel can be seen to have segregated to an area corresponding to the area of darker contrast in a).

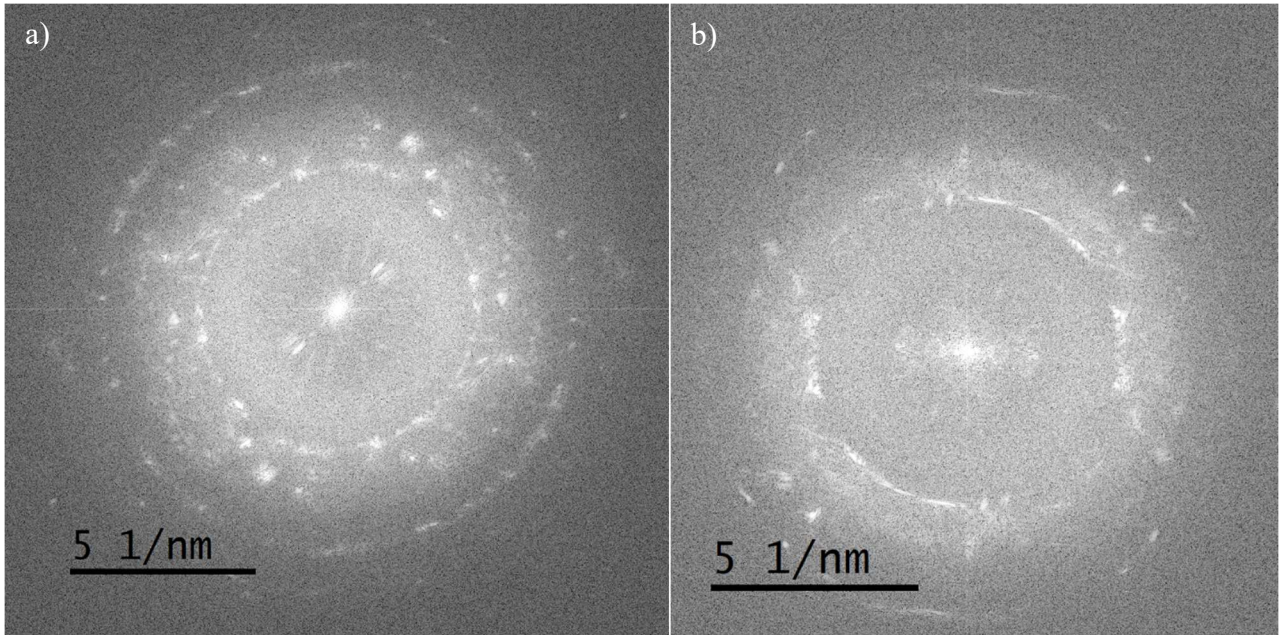


Figure 28: a) Fourier transform of Figure 26a. b) Fourier transform of Figure 27a.

## 6. Discussion

For the oxidised samples, the presence of  $\beta$ -NiMoO<sub>4</sub> in the early stages of oxidation (when sintering is at a minimum in bulk samples), combined with the almost exclusive observation of  $\beta$ -NiMoO<sub>4</sub> in size-selected (and thus isolated) nanoparticles suggests that  $\beta$ -NiMoO<sub>4</sub> may be preferentially formed when domains are sufficiently small and/or isolated. Whether this is for kinetic or thermodynamic (i.e., size effects) reasons is unclear. Furthermore, the structure of the unknown Ni-Mo phase exhibited in the as-deposited particles may play a role.

Nevertheless, this observation would neatly explain previous results indicating that an active phase synthesised from  $\beta$ -NiMoO<sub>4</sub> yield higher activity than  $\alpha$ -NiMoO<sub>4</sub> [14-16], even for sulfided catalysts where the original oxide is no longer present [15]; given the above, the effect can be interpreted as the successful synthesis of  $\beta$ -NiMoO<sub>4</sub> being indicative of higher dispersion of the active phase in the catalyst support and thus larger catalyst surface area. The deviant behaviour of the  $\beta$ -NiMoO<sub>4</sub> 220 peak at 400 °C can likely be explained by the low temperature inhibiting sintering combined with the fact that the 4 h sample had only half the particle surface density compared to the other samples of the same series. The latter would further hinder sintering and thus, under this hypothesis, also the loss of  $\beta$ -NiMoO<sub>4</sub>.

The complete absence of observable MoO<sub>3</sub> in the oxidised size-selected samples can be explained by generated  $\alpha$ -MoO<sub>3</sub> (likely chiefly from the pure Mo part of the Janus particles in the as-deposited case) sublimating. Since the sample volume is extremely small compared to the furnaces used, even at temperatures such as 400 °C, where the equilibrium  $\alpha$ -MoO<sub>3</sub> pressure is low [51], the complete sublimation of  $\alpha$ -MoO<sub>3</sub> can be considered likely. In contrast, in commercial catalysts the diffusion limitations imposed by the microporous nature of the support likely aids in retention of pure  $\alpha$ -MoO<sub>3</sub>, thus making essentially arbitrary Ni-Mo ratios possible. As such, the viability of spark discharge generated nanoparticles as a model system is likely limited to Ni-Mo catalysts with, at best, a slight excess of Mo (cf. the particle in Figure 21).

The behaviour of the particles in a reducing environment is, as mentioned, largely consistent with previous literature on and phenomena observed for larger “bulk” NiMoO<sub>4</sub> samples. While no morphological change could be observed at 400 °C, considering previous data on the activity of reduced Ni-Mo catalysts [11, 62], the possibility remains that some extent of reduction has occurred on the very surface of the nanoparticles. Although the resolution of the microscope in principle should allow for atomic-layer resolution, a structural change that penetrates only a handful of layers into the material may be hard to observe and/or interpret, and characterisation using a surface-sensitive or highly-resolved spectroscopic technique may be necessary.

In contrast, the results for particles reduced at 710 °C are a relatively clear indication that reduction does take place. Previous XPS results indicated a failure to observe Mo(IV) but did observe the reduction of Ni(II) to Ni(0) [83], which is broadly consistent with the morphological changes observed here. As the author of that work carried out reduction for only 1 h, it is possible that the failure to observe Mo(IV) can be attributed simply to the kinetics of the reaction. If the interpretation of the Moiré fringes at the edges of the particle in

Figure 26 as indicative of a structural change from  $\text{MoO}_3$  to  $\text{MoO}_2$  is correct, even at 2 h of reduction, the change from Mo(VI) to Mo(IV) only penetrates a few atomic layers deep. Furthermore, the XEDS map in Figure 26b indicates that there is still residual Ni in the Mo matrix, meaning that the central structure may be arrested in some sort of intermediate between  $\text{NiMoO}_4$  and  $\text{MoO}_3$ . Both of these observations make it likely that the progress of reduction might be minimal at 1 h as compared to 2 h. For example, what is here observed as an Mo-rich matrix might be present as some sort of Ni-deficient  $\text{NiMoO}_4$ -like structure. This would also explain why the Ni:Mo ratio does not change during reduction as it did during oxidation: if Mo is never present as  $\text{MoO}_3$ , it will not sublime, thus preserving the overall particle composition.

For the unoxidized samples, the ability to directly link the observed unindexed peaks in the PXRD pattern with observable periodicities in TEM imaging strongly suggest that the unindexed peaks are due to some sort of new Ni-Mo phase, rather than being caused by impurities in the sample. For example, the phase might be some sort of non-equilibrium phase generated via rapid cooling of the nanoparticles when they impinge on the room temperature deposition substrate after having been compacted at 1200 °C, or alternatively already as an aerosol when they exit the furnace. The failure of *ab initio* indexation methods to generate well-fitting structure might further indicate that there are in fact multiple such phases present. This could for example be caused by differences in heat transfer depending on whether the particle is deposited directly onto the substrate or onto an already present layer of nanoparticles, or be due to differences in overall composition between individual nanoparticles. However, more powerful methods than trial-and-error exclusion of diffraction peaks are necessary to elucidate the details of these structures in this case, for example molecular dynamics modelling of the cooling process to generate feasible candidate structures that can then be matched towards the real spectra.

## 7. Summary and Conclusions

- Spark-discharge generated nanoparticles can be used as a model for Ni-Mo catalyst active sites up to a slight excess of Mo in the active phase.
- Size-selected deposition allows for the study of oxidation phenomena in the absence of sintering.
- The enhanced activity of  $\beta$ -NiMoO<sub>4</sub> compared to the corresponding  $\alpha$ -polymorph may be caused by small and dispersed active phase particles favouring the formation of the  $\beta$ -polymorph. In this case, the effect arises not necessarily from than any catalytic property of  $\beta$ -NiMoO<sub>4</sub> as such, but from the higher surface area afforded by the smaller active phase particles.
- Reduction of the particles show no indication of size effects; previous failures to observe a change from Mo(VI) to Mo(IV) may thus be attributed to slow reaction kinetics rather than, e.g., size effects.
- The conditions of the spark discharge generation lead to the formation of one or more new Ni-Mo phases with a well-defined, although as yet undetermined, crystal structure.

## 8. Outlook

In this work, the analysis presented of the oxidation and reduction phenomena is *ex situ* and post-mortem in nature. Brief attempts were made at environmental TEM (ETEM) studies of oxidation and reduction phenomena, in order to be able to directly relate compositions and morphology before and after the processes. However, as bulk samples (see “4.1. Sample synthesis and preparation”) were used rapid and heavy sintering of the particles prevented any meaningful analysis; experiments with size-selected ETEM samples were hindered by breakdown of the available environmental transmission electron microscope. A highly relevant avenue for further work is therefore the *in situ* study of oxidation and reduction phenomena in size-selected, isolated particles.

As mentioned in section 7., determination of the unknown structure(s) in the as-deposited nanoparticles also remains as a field of further study. If the hypothesis of the unknown structure(s) arising from rapid cooling is correct, molecular dynamics simulations of such cooling may provide suitable candidate structures to match with experimental diffraction patterns. However, if the phases are indeed hitherto unknown, it is possible that some experimental re-evaluation of the Ni-Mo phase diagram may need to be performed in the context of nanoparticles, since any thermodynamic modelling will inevitably build upon previously available experimental phase diagrams. For example, a series of particle depositions with finely graded compositional changes in the Ni-Mo content of the electrodes could be conducted to see if and when the observed phases match with the predictions of currently available phase diagram.

Further studies of the reduction of the nanoparticles are also called for. In particular, spectroscopic investigation of oxidation state of Mo in the particles reduced at 400 °C is highly relevant (for example via EELS or XPS), as the lack of visible morphological change throughout the particle may not capture reduction occurring only in the surface layer in the nanoparticles. Furthermore, while the current set of oxidation and reduction experiments indicate that the composition of the particles is by and large stable during oxidation and subsequent reduction, cycling of reducing and oxidising environments could be used to characterise the long-term stability of the catalyst composition and to some extent simulate the effects of extensive catalytic cycling. Finally, longer reduction times could be used in order to stimulate grain growth and make TEM analysis of the formed structures easier.

## 9. References

- [1] IEA, "Net Zero by 2050," Paris, 2021. Accessed: 20 Jan 2022. [Online]. Available: <https://www.iea.org/reports/net-zero-by-2050>
- [2] M. B. Jones, "Biofuel Developments in Central Africa: Technology Transfer from Ireland," in *Energy for Rural and Island Communities*, J. Twidell, F. Riddoch, and B. Grainger Eds.: Pergamon, 1984, pp. 355-361.
- [3] M. Giampietro, S. Ulgiati, and D. Pimentel, "Feasibility of Large-Scale Biofuel Production," *BioScience*, vol. 47, no. 9, pp. 587-600, Oct 1997, doi: 10.2307/1313165.
- [4] R. E. H. Sims, W. Mabee, J. N. Saddler, and M. Taylor, "An overview of second generation biofuel technologies," *Bioresource Technology*, vol. 101, no. 6, pp. 1570-1580, 2010/03/01/ 2010, doi: <https://doi.org/10.1016/j.biortech.2009.11.046>.
- [5] M. V. Rodionova *et al.*, "Biofuel production: Challenges and opportunities," *International Journal of Hydrogen Energy*, vol. 42, no. 12, pp. 8450-8461, 2017/03/23/ 2017, doi: <https://doi.org/10.1016/j.ijhydene.2016.11.125>.
- [6] J. A. Moulijn, M. Makkee, and A. v. Diepen, *Chemical process technology*, Second edition. ed. Chichester, West Sussex, United Kingdom: John Wiley & Sons Ltd., 2013, pp. xiv, 552 pages.
- [7] P. M. Mortensen, J. D. Grunwaldt, P. A. Jensen, K. G. Knudsen, and A. D. Jensen, "A review of catalytic upgrading of bio-oil to engine fuels," *Applied Catalysis A: General*, vol. 407, no. 1, pp. 1-19, Nov 4 2011, doi: <https://doi.org/10.1016/j.apcata.2011.08.046>.
- [8] E. Laurent and B. Delmon, "Study of the hydrodeoxygenation of carbonyl, carboxylic and guaiacyl groups over sulfided CoMo/ $\gamma$ -Al<sub>2</sub>O<sub>3</sub> and NiMo/ $\gamma$ -Al<sub>2</sub>O<sub>3</sub> catalysts: I. Catalytic reaction schemes," *Applied Catalysis A: General*, vol. 109, no. 1, pp. 77-96, Feb 17 1994, doi: [https://doi.org/10.1016/0926-860X\(94\)85004-6](https://doi.org/10.1016/0926-860X(94)85004-6).
- [9] R. J. French, J. Stunkel, S. Black, M. Myers, M. M. Yung, and K. Lisa, "Evaluate Impact of Catalyst Type on Oil Yield and Hydrogen Consumption from Mild Hydrotreating," *Energy & Fuels*, vol. 28, no. 5, pp. 3086-3095, 2014/05/15 2014, doi: 10.1021/ef4019349.
- [10] P. Kumar, S. K. Maity, and D. Shee, "Role of NiMo Alloy and Ni Species in the Performance of NiMo/Alumina Catalysts for Hydrodeoxygenation of Stearic Acid: A Kinetic Study," *ACS Omega*, vol. 4, no. 2, pp. 2833-2843, Feb 28 2019, doi: 10.1021/acsomega.8b03592.
- [11] H. Ojagh, "Hydrodeoxygenation (HDO) catalysts - Characterization, reaction and deactivation studies," PhD, Department of Chemistry and Chemical Engineering, Chalmers University of Technology, Gothenburg, Sweden, 978-91-7597-704-1, 2018. [Online]. Available: <https://research.chalmers.se/publication/500901>
- [12] J. V. Lauritsen *et al.*, "Atomic-Scale Structure of Co-Mo-S Nanoclusters in Hydrotreating Catalysts," *Journal of Catalysis*, vol. 197, no. 1, pp. 1-5, 2001/01/01/ 2001, doi: <https://doi.org/10.1006/jcat.2000.3088>.
- [13] J. L. Brito, J. Laine, and K. C. Pratt, "Temperature-programmed reduction of Ni-Mo oxides," *Journal of Materials Science*, vol. 24, no. 2, pp. 425-431, Feb 1 1989, doi: 10.1007/BF01107422.
- [14] S. Baoyi, X. Aiju, and W. Jiang, "The impact of preparation methods on the structure and catalytic performance of NiMoO<sub>4</sub> for oxidative dehydrogenation of propane," *Integrated Ferroelectrics*, vol. 171, no. 1, pp. 16-22, May 3 2016, doi: 10.1080/10584587.2016.1169085.
- [15] J. n. L. Brito and A. L. Barbosa, "Effect of Phase Composition of the Oxidic Precursor on the HDS Activity of the Sulfided Molybdates of Fe(II), Co(II), and Ni(II)," *Journal of Catalysis*, vol. 171, no. 2, pp. 467-475, Oct 15 1997, doi: <https://doi.org/10.1006/jcat.1997.1796>.
- [16] J. A. Rodriguez, S. Chaturvedi, J. C. Hanson, A. Albornoz, and J. L. Brito, "Electronic Properties and Phase Transformations in CoMoO<sub>4</sub> and NiMoO<sub>4</sub>: XANES and Time-Resolved Synchrotron XRD Studies," *The Journal of Physical Chemistry B*, vol. 102, no. 8, pp. 1347-1355, Feb 1 1998, doi: 10.1021/jp972137q.

- [17] S. Blomberg *et al.*, "Bimetallic Nanoparticles as a Model System for an Industrial NiMo Catalyst," *Materials*, vol. 12, no. 22, p. 3727, 2019. [Online]. Available: <https://www.mdpi.com/1996-1944/12/22/3727>.
- [18] K. Frisk, "A thermodynamic evaluation of the Mo-Ni system," *Calphad*, vol. 14, no. 3, pp. 311-320, Jul 1 1990, doi: [https://doi.org/10.1016/0364-5916\(90\)90031-T](https://doi.org/10.1016/0364-5916(90)90031-T).
- [19] R. E. W. Casselton and W. Hume-Rothery, "The equilibrium diagram of the system molybdenum-nickel," *Journal of the Less Common Metals*, vol. 7, no. 3, pp. 212-221, Sep 1 1964, doi: [https://doi.org/10.1016/0022-5088\(64\)90068-2](https://doi.org/10.1016/0022-5088(64)90068-2).
- [20] W. P. Davey, "Precision Measurements of the Lattice Constants of Twelve Common Metals," *Physical Review*, vol. 25, no. 6, pp. 753-761, Jun 1 1925, doi: 10.1103/PhysRev.25.753.
- [21] D. Harker, "The Crystal Structure of Ni<sub>4</sub>Mo," *The Journal of Chemical Physics*, vol. 12, no. 7, pp. 315-317, 1944, doi: 10.1063/1.1723945.
- [22] G. Van Tendeloo and S. Amelinckx, "The domain structure of the  $\delta$ -phase alloy NiMo," *Materials Research Bulletin*, vol. 8, no. 6, pp. 721-731, Jun 1 1973, doi: [https://doi.org/10.1016/0025-5408\(73\)90066-4](https://doi.org/10.1016/0025-5408(73)90066-4).
- [23] C. B. Shoemaker and D. P. Shoemaker, "The crystal structure of the [ $\delta$ ] phase Mo-Ni," *Acta Crystallographica*, vol. 16, no. 10, pp. 997-1009, 1963, doi: doi:10.1107/S0365110X63002668.
- [24] A. K. Cheetham and D. A. O. Hope, "Magnetic ordering and exchange effects in the antiferromagnetic solid solutions Mn<sub>x</sub>Ni(1-x)O," *Physical Review B*, vol. 27, no. 11, pp. 6964-6967, Jun 1 1983, doi: 10.1103/PhysRevB.27.6964.
- [25] S. Dey, S. Bhattacharjee, M. G. Chaudhuri, R. S. Bose, S. Halder, and C. K. Ghosh, "Synthesis of pure nickel(iii) oxide nanoparticles at room temperature for Cr(vi) ion removal," *RSC Advances*, 10.1039/C5RA05810D vol. 5, no. 67, pp. 54717-54726, 2015, doi: 10.1039/C5RA05810D.
- [26] A. Jain *et al.*, "The Materials Project: A materials genome approach to accelerating materials innovation," *APL Materials*, vol. 1, no. 1, p. 011002, 2013, doi: 10.1063/1.4812323.
- [27] I. A. de Castro *et al.*, "Molybdenum Oxides – From Fundamentals to Functionality," *Advanced Materials*, vol. 29, no. 40, p. 1701619, 2017, doi: <https://doi.org/10.1002/adma.201701619>.
- [28] L. E. M. Smart, Elaine A., *Solid State Chemistry: An Introduction*, 4th ed. Boca Raton, Florida, United States of America: CRC Press, 2012.
- [29] P. F. Carcia and E. M. McCarron, "Synthesis and properties of thin film polymorphs of molybdenum trioxide," *Thin Solid Films*, vol. 155, no. 1, pp. 53-63, Dec 15 1987, doi: [https://doi.org/10.1016/0040-6090\(87\)90452-4](https://doi.org/10.1016/0040-6090(87)90452-4).
- [30] A. Chithambararaj and A. C. Bose, "Hydrothermal synthesis of hexagonal and orthorhombic MoO<sub>3</sub> nanoparticles," *Journal of Alloys and Compounds*, vol. 509, no. 31, pp. 8105-8110, Aug 4 2011, doi: <https://doi.org/10.1016/j.jallcom.2011.05.067>.
- [31] M. Zoller, M. O'Sullivan, and H. Huppertz, "On the Reduction of MoO<sub>3</sub> to MoO<sub>2</sub>: A Path to Control the Particle Size and Morphology," *Chemistry – A European Journal*, vol. 27, no. 72, pp. 18141-18149, 2021, doi: <https://doi.org/10.1002/chem.202103417>.
- [32] E. Lalik, W. I. F. David, P. Barnes, and J. F. C. Turner, "Mechanisms of Reduction of MoO<sub>3</sub> to MoO<sub>2</sub> Reconciled?," *The Journal of Physical Chemistry B*, vol. 105, no. 38, pp. 9153-9156, 2001/09/01 2001, doi: 10.1021/jp011622p.
- [33] A. A. Magnéli, Georg, "On the MoO<sub>2</sub> structure type," *Acta Chemica Scandinavica*, vol. 9, pp. 1378-1381, 1955, doi: 10.3891/acta.chem.scand.09-1378.
- [34] L. Yang *et al.*, "Structure and effective visible-light-driven photocatalytic activity of  $\alpha$ -NiMoO<sub>4</sub> for degradation of methylene blue dye," *Journal of Alloys and Compounds*, vol. 664, pp. 756-763, Apr 15 2016, doi: <https://doi.org/10.1016/j.jallcom.2015.10.037>.
- [35] J. L. Brito, A. L. Barbosa, A. Albornoz, F. Severino, and J. Laine, "Nickel molybdate as precursor of HDS catalysts: Effect of phase composition," *Catalysis Letters*, vol. 26, no. 3, pp. 329-337, Sep 1 1994, doi: 10.1007/BF00810606.

- [36] R. A. Madeley and S. E. Wanke, "Variation of the dispersion of active phases in commercial nickel—molybdenum/ $\gamma$ -alumina hydrotreating catalysts during oxidative regeneration," *Applied Catalysis*, vol. 39, pp. 295-314, May 16 1988, doi: [https://doi.org/10.1016/S0166-9834\(00\)80956-2](https://doi.org/10.1016/S0166-9834(00)80956-2).
- [37] B. Schonfeld, J. J. Huang, and S. C. Moss, "Anisotropic mean-square displacements (MSD) in single-crystals of 2H- and 3R-MoS<sub>2</sub>," *Acta Crystallographica Section B*, vol. 39, no. 4, pp. 404-407, Aug 1 1983, doi: doi:10.1107/S0108768183002645.
- [38] L. Kihlborg, "Least squares refinement of the crystal structure of molybdenum trioxide," *Arkiv för Kemi*, vol. 21, no. 34, pp. 357-364, 1963.
- [39] E. M. McCarron, " $\beta$ -MoO<sub>3</sub>: a metastable analogue of WO<sub>3</sub>," *Journal of the Chemical Society, Chemical Communications*, 10.1039/C39860000336 no. 4, pp. 336-338, 1986, doi: 10.1039/C39860000336.
- [40] Ø. S. Fjellvåg, A. Ruud, H. H. Sønsteby, O. Nilsen, and H. Fjellvåg, "Crystallization, Phase Stability, and Electrochemical Performance of  $\beta$ -MoO<sub>3</sub> Thin Films," *Crystal Growth & Design*, vol. 20, no. 6, pp. 3861-3866, Jun 3 2020, doi: 10.1021/acs.cgd.0c00156.
- [41] C. C. Zhang *et al.*, "Raman studies of hexagonal MoO<sub>3</sub> at high pressure," *physica status solidi (b)*, vol. 248, no. 5, pp. 1119-1122, Mar 23 2011, doi: <https://doi.org/10.1002/pssb.201000633>.
- [42] A. P. de Moura *et al.*, "Structural, Optical, and Magnetic Properties of NiMoO<sub>4</sub> Nanorods Prepared by Microwave Sintering," *The Scientific World Journal*, vol. 2015, p. 315084, Feb 23 2015, doi: 10.1155/2015/315084.
- [43] K. D. Bronsema, J. L. De Boer, and F. Jellinek, "On the structure of molybdenum diselenide and disulfide," *Zeitschrift für anorganische und allgemeine Chemie*, vol. 540, no. 9-10, pp. 15-17, Sep 1 1986, doi: <https://doi.org/10.1002/zaac.19865400904>.
- [44] S. Saito and P. A. Beck, "The crystal structure of MoNi<sub>3</sub>," *Transactions of the American Institute of Mining and Metallurgical Engineers*, vol. 215, no. 6, pp. 938-941, 1959.
- [45] N. Smith, "The Structure of Thin Films of Metallic Oxides and Hydrates," *Journal of the American Chemical Society*, vol. 58, no. 1, pp. 173-179, 1936/01/01 1936, doi: 10.1021/ja01292a050.
- [46] A. Bolzan, B. Kennedy, and C. Howard, "Neutron Powder Diffraction Study of Molybdenum and Tungsten Dioxides," *Australian Journal of Chemistry*, vol. 48, no. 8, pp. 1473-1477, 1995, doi: <https://doi.org/10.1071/CH9951473>.
- [47] R. H. Bricknell and D. A. Woodford, "The mechanism of cavity formation during high temperature oxidation of nickel," *Acta Metallurgica*, vol. 30, no. 1, pp. 257-264, Jan 1 1982, doi: [https://doi.org/10.1016/0001-6160\(82\)90064-5](https://doi.org/10.1016/0001-6160(82)90064-5).
- [48] S. Mrowec and Z. Grzesik, "Oxidation of nickel and transport properties of nickel oxide," *Journal of Physics and Chemistry of Solids*, vol. 65, no. 10, pp. 1651-1657, Oct 1 2004, doi: <https://doi.org/10.1016/j.jpcs.2004.03.011>.
- [49] R. Haugsrud, "On the high-temperature oxidation of nickel," *Corrosion Science*, vol. 45, no. 1, pp. 211-235, Jan 1 2003, doi: [https://doi.org/10.1016/S0010-938X\(02\)00085-9](https://doi.org/10.1016/S0010-938X(02)00085-9).
- [50] J. G. Railsback, A. C. Johnston-Peck, J. Wang, and J. B. Tracy, "Size-Dependent Nanoscale Kirkendall Effect During the Oxidation of Nickel Nanoparticles," *ACS Nano*, vol. 4, no. 4, pp. 1913-1920, Apr 27 2010, doi: 10.1021/nn901736y.
- [51] G. De Micco, H. Nassini, and A. Bohé, "Kinetics of molybdenum oxidation between 375 and 500°C," in *Molybdenum and its compounds: Applications, electrochemical properties and geological implications*, V. S. L. Saji, Sergey I. Ed. New York: Nova Science Publishers Inc., 2014, pp. 313-338.
- [52] E. I. Steifel, "Molybdenum and Molybdenum Alloys," in *Kirk - Othmer Encyclopedia of Chemical Technology*, pp. 1-16.
- [53] E. I. Steifel, "Molybdenum Compounds," in *Kirk - Othmer Encyclopedia of Chemical Technology*, pp. 1-24.

- [54] J. H. DeVan, "Catastrophic oxidation of high-temperature alloys," Oak Ridge National Laboratory, United States of America, Nov 10 1961. [Online]. Available: <https://www.osti.gov/biblio/4826329>
- [55] S. S. Brenner, "Oxidation of Iron-Molybdenum and Nickel-Molybdenum Alloys," *Journal of The Electrochemical Society*, vol. 102, no. 1, p. 7, 1955, doi: 10.1149/1.2429990.
- [56] R. B. Patil, S. D. House, A. Mantri, J. C. Yang, and J. R. McKone, "Direct Observation of Ni–Mo Bimetallic Catalyst Formation via Thermal Reduction of Nickel Molybdate Nanorods," *ACS Catalysis*, vol. 10, no. 18, pp. 10390-10398, Sep 18 2020, doi: 10.1021/acscatal.0c02264.
- [57] J. A. Rodriguez, J. Y. Kim, J. C. Hanson, and J. L. Brito, "Reduction of CoMoO<sub>4</sub> and NiMoO<sub>4</sub>: in situ Time-Resolved XRD Studies," *Catalysis Letters*, vol. 82, no. 1, pp. 103-109, Sep 1 2002, doi: 10.1023/A:1020556528042.
- [58] J. Wildschut, F. H. Mahfud, R. H. Venderbosch, and H. J. Heeres, "Hydrotreatment of Fast Pyrolysis Oil Using Heterogeneous Noble-Metal Catalysts," *Industrial & Engineering Chemistry Research*, vol. 48, no. 23, pp. 10324-10334, Dec 12 2009, doi: 10.1021/ie9006003.
- [59] M. Zdražil, "MgO-supported Mo, CoMo and NiMo sulfide hydrotreating catalysts," *Catalysis Today*, vol. 86, no. 1, pp. 151-171, Nov 1 2003, doi: [https://doi.org/10.1016/S0920-5861\(03\)00409-7](https://doi.org/10.1016/S0920-5861(03)00409-7).
- [60] D. Ferdous, A. K. Dalai, and J. Adjaye, "A series of NiMo/Al<sub>2</sub>O<sub>3</sub> catalysts containing boron and phosphorus: Part I. Synthesis and characterization," *Applied Catalysis A: General*, vol. 260, no. 2, pp. 137-151, Apr 8 2004, doi: <https://doi.org/10.1016/j.apcata.2003.10.010>.
- [61] A. J. van Dillen, R. J. A. M. Terörde, D. J. Lensveld, J. W. Geus, and K. P. de Jong, "Synthesis of supported catalysts by impregnation and drying using aqueous chelated metal complexes," *Journal of Catalysis*, vol. 216, no. 1, pp. 257-264, May 1 2003, doi: [https://doi.org/10.1016/S0021-9517\(02\)00130-6](https://doi.org/10.1016/S0021-9517(02)00130-6).
- [62] M. Grilc, B. Likozar, and J. Levec, "Hydrodeoxygenation and hydrocracking of solvolysed lignocellulosic biomass by oxide, reduced and sulphide form of NiMo, Ni, Mo and Pd catalysts," *Applied Catalysis B: Environmental*, vol. 150-151, pp. 275-287, May 5 2014, doi: <https://doi.org/10.1016/j.apcatb.2013.12.030>.
- [63] S. Ding, S. Jiang, Y. Zhou, Q. Wei, and W. Zhou, "Catalytic characteristics of active corner sites in CoMoS nanostructure hydrodesulfurization – A mechanism study based on DFT calculations," *Journal of Catalysis*, vol. 345, pp. 24-38, Jan 1 2017, doi: <https://doi.org/10.1016/j.jcat.2016.11.011>.
- [64] X. Wang and U. S. Ozkan, "Characterization of Active Sites over Reduced Ni–Mo/Al<sub>2</sub>O<sub>3</sub> Catalysts for Hydrogenation of Linear Aldehydes," *The Journal of Physical Chemistry B*, vol. 109, no. 5, pp. 1882-1890, Feb 1 2005, doi: 10.1021/jp046489q.
- [65] S. Schwyn, E. Garwin, and A. Schmidt-Ott, "Aerosol generation by spark discharge," *Journal of Aerosol Science*, vol. 19, no. 5, pp. 639-642, Oct 1 1988, doi: [https://doi.org/10.1016/0021-8502\(88\)90215-7](https://doi.org/10.1016/0021-8502(88)90215-7).
- [66] E. O. Knutson and K. T. Whitby, "Aerosol classification by electric mobility: apparatus, theory, and applications," *Journal of Aerosol Science*, vol. 6, no. 6, pp. 443-451, Nov 1 1975, doi: [https://doi.org/10.1016/0021-8502\(75\)90060-9](https://doi.org/10.1016/0021-8502(75)90060-9).
- [67] V. K. P. P. Y. Zavalij, "Fundamentals of Diffraction," in *Fundamentals of Powder Diffraction and Structural Characterization of Materials*. Boston, MA: Springer US, 2009, pp. 133-149.
- [68] V. K. P. P. Y. Zavalij, "The Powder Diffraction Pattern," in *Fundamentals of Powder Diffraction and Structural Characterization of Materials*. Boston, MA: Springer US, 2009, pp. 151-202.
- [69] D. Louër and M. Louër, "Méthode d'essais et erreurs pour l'indexation automatique des diagrammes de poudre," *Journal of Applied Crystallography*, vol. 5, no. 4, pp. 271-275, Aug 1 1972, doi: <https://doi.org/10.1107/S0021889872009483>.
- [70] V. K. P. P. Y. Zavalij, "Determination and Refinement of the Unit Cell," in *Fundamentals of Powder Diffraction and Structural Characterization of Materials*. Boston, MA: Springer US, 2009, pp. 407-495.

- [71] A. Boulouf and D. Louër, "Indexing of powder diffraction patterns for low-symmetry lattices by the successive dichotomy method," *Journal of Applied Crystallography*, vol. 24, no. 6, pp. 987-993, Dec 1 1991, doi: <https://doi.org/10.1107/S0021889891006441>.
- [72] P. M. De Wolff, "A simplified criterion for the reliability of a powder pattern indexing," *Journal of Applied Crystallography*, vol. 1, no. 2, pp. 108-113, Jun 2 1968, doi: <https://doi.org/10.1107/S002188986800508X>.
- [73] A. L. Patterson, "The Scherrer Formula for X-Ray Particle Size Determination," *Physical Review*, vol. 56, no. 10, pp. 978-982, 11/15/ 1939, doi: 10.1103/PhysRev.56.978.
- [74] R. E. Smallman and A. H. W. Ngan, "Chapter 5 - Characterization and Analysis," in *Modern Physical Metallurgy (Eighth Edition)*, R. E. Smallman and A. H. W. Ngan Eds. Oxford: Butterworth-Heinemann, 2014, pp. 159-250.
- [75] D. B. Williams and C. B. Carter, "The Transmission Electron Microscope," in *Transmission Electron Microscopy: A Textbook for Materials Science*. Boston, MA: Springer US, 2009, pp. 3-22.
- [76] D. B. Williams and C. B. Carter, "Inelastic Scattering and Beam Damage," in *Transmission Electron Microscopy: A Textbook for Materials Science*, D. B. Williams and C. B. Carter Eds. Boston, MA: Springer US, 2009, pp. 53-71.
- [77] D. B. Williams and C. B. Carter, "Phase-Contrast Images," in *Transmission Electron Microscopy: A Textbook for Materials Science*. Boston, MA: Springer US, 2009, pp. 389-405.
- [78] D. B. Williams and C. B. Carter, "X-ray Spectrometry," in *Transmission Electron Microscopy: A Textbook for Materials Science*. Boston, MA: Springer US, 2009, pp. 581-603.
- [79] M. E. Messing, K. A. Dick, L. R. Wallenberg, and K. Deppert, "Generation of size-selected gold nanoparticles by spark discharge — for growth of epitaxial nanowires," *Gold Bulletin*, vol. 42, no. 1, pp. 20-26, 2009/03/01 2009, doi: 10.1007/BF03214902.
- [80] N. Doebelin and R. Kleeberg, "Profex: a graphical user interface for the Rietveld refinement program BGMN," *Journal of Applied Crystallography*, vol. 48, no. 5, pp. 1573-1580, Aug 29 2015, doi: doi:10.1107/S1600576715014685.
- [81] G. Bergerhoff, I. Brown, and F. Allen, "Crystallographic databases," *International Union of Crystallography, Chester*, vol. 360, pp. 77-95, 1987.
- [82] V. Petříček, M. Dušek, and L. Palatinus, "Crystallographic Computing System JANA2006: General features," *Zeitschrift für Kristallographie - Crystalline Materials*, vol. 229, no. 5, pp. 345-352, May 2014, doi: doi:10.1515/zkri-2014-1737.
- [83] H. Makhool, "Generation of Model NiMo Hydrotreating Nano-catalysts via the Spark Discharge Technique," M.Sc.Eng. Master's Thesis, Chemical Engineering, Lund University, Lund, 2020. [Online]. Available: <http://lup.lub.lu.se/student-papers/record/9014275>
- [84] C. Wagner, "Beitrag zur Theorie des Anlaufvorgangs," *Zeitschrift für Physikalische Chemie*, vol. 21B, no. 1, pp. 25-41, Feb 1 1933, doi: doi:10.1515/zpch-1933-2105.
- [85] R. E. Smallman and A. H. W. Ngan, "Chapter 16 - Oxidation, Corrosion and Surface Engineering," in *Modern Physical Metallurgy (Eighth Edition)*, R. E. Smallman and A. H. W. Ngan Eds. Oxford: Butterworth-Heinemann, 2014, pp. 617-657.
- [86] A. T. Fromhold, "Growth rate of low-space-charge oxides on spherical metal particles," *Journal of Physics and Chemistry of Solids*, vol. 49, no. 10, pp. 1159-1166, Jan 1 1988, doi: [https://doi.org/10.1016/0022-3697\(88\)90170-9](https://doi.org/10.1016/0022-3697(88)90170-9).
- [87] R. Karmhag, T. Tesfamichael, E. Wäckelgård, G. A. Niklasson, and M. Nygren, "Oxidation Kinetics of Nickel Particles: Comparison Between Free Particles and Particles in an Oxide Matrix," *Solar Energy*, vol. 68, no. 4, pp. 329-333, Jan 1 2000, doi: [https://doi.org/10.1016/S0038-092X\(00\)00025-6](https://doi.org/10.1016/S0038-092X(00)00025-6).
- [88] L. Olbjer, *Experimentell och industriell statistik*. Lund: Faculty of Engineering, Lund University (in Swedish), 2000.



## 10.A. Appendix A – Parabolic rate laws

The kinetics of metal oxidation can often be quantified in terms of a parabolic rate law first proposed by Wagner in 1933 [84-86]:

$$L^2 - L_0^2 = 2k_p t \quad (A1)$$

where  $L$  is the thickness of the oxide film formed on a foil sample,  $t$  is the time and  $k_p$  is termed the parabolic rate constant; the entire expression is referred to as a *parabolic rate law*. The factor 2 is utilised in this text following Fromhold [86]. More specifically, this is a steady-state solution to Fick's law for the diffusion of charged point defects, assuming constant diffusivities and an effective zero electric field [87]. For small spherical particles, this is modified to [86, 87]

$$k_p t = \frac{zr_0^2}{2(z-1)} \left[ z - (z-1)(1-x)^{2/3} - (1+(z-1)x)^{2/3} \right] \quad (A2)$$

where  $z$  is the volumetric ratio between the oxide and the base metal,  $r_0$  is the initial particle radius, and  $x$  is the fractional yield of oxide (i.e.,  $x = 1$  when the particle is fully oxidised). If neglecting the volumetric change between oxide and metal (i.e., setting  $z = 1$ ), eq. 2 can be rewritten in terms of the thickness of the oxide film as [86]

$$\frac{1}{2}L^2 - \frac{1}{3r_0}L^3 = k_p t. \quad (A3)$$

In this model,  $L$  never exceeds  $r_0$ , and so the rate law is well-behaved.

## 10.B. Appendix B – Gauss’s approximation formula and error propagation to atomic percentages

For a function  $g(X)$  of a stochastic variable  $X$  with expectation value  $\mu$  and variance  $\sigma^2$ , the expectation value  $E(g(X))$  and variance  $V(g(X))$  can be approximated by [88]:

$$E(g(X)) \approx g(\mu) + (X - \mu)g'(\mu) \quad (B1)$$

$$V(g(X)) \approx [g'(\mu)]^2 V(X) \quad (B2)$$

For a mixture of two elements A and B, the atomic percentage of A  $x$  can be expressed in terms of the weight percentage of A  $w$  according to

$$x = \frac{w/M_A}{w/M_A + (1-w)/M_B} = \frac{w}{\left(1 - \frac{M_A}{M_B}\right)w + \frac{M_A}{M_B}}, \quad (B3)$$

where  $M_i$  are molar masses of the elements. The derivative  $x' = \frac{dx}{dw}$  then becomes

$$x' = \frac{M_A/M_B}{\left(\left(1 - \frac{M_A}{M_B}\right)w + \frac{M_A}{M_B}\right)^2} \quad (B4)$$

and an estimate of the variance  $\sigma_x^2$  in terms of  $\sigma_w^2$  becomes, using eq. B2,

$$\sigma_x^2 = \frac{(M_A/M_B)^2}{\left(\left(1 - \frac{M_A}{M_B}\right)w + \frac{M_A}{M_B}\right)^4} \sigma_w^2. \quad (B5)$$